

Experimental proposal for the Dynamical Space-time approach to wavefunction collapse

Garrelt Quandt-Wiese ¹

Schlesierstr. 16, 64297 Darmstadt, Germany

garrelt@quandt-wiese.de

<http://www.quandt-wiese.de>

An experiment for checking the Dynamical Spacetime approach to wavefunction collapse is proposed. The Dynamical Spacetime approach predicts deviations from Born's rule, when a solid evolves into a three-state superposition, and when the displacement between the superposed states is, at the reduction point in time, significantly larger than the spatial variation of the solids nuclei, being typically on the order of a tenth of an Ångström. The solid is brought into the three-state superposition by splitting a photon into three beams and by detecting it in each beam by avalanche photodiodes, which displace the solid at different distances with the help of a piezoactuator. The challenge of the experiment is the precise prediction of the setup's reduction point in time to ensure a sufficient separation between the states at this point in time. This is addressed by avoiding interactions of the setup with the environment during superposition, and by a precise calculation of the setup's reduction point in time with the help of a formulary for the Diósi-Penrose criterion for solids in quantum superpositions. Since the measurement of reduction probabilities is not disturbed by state decoherence, the experiment can be performed at room temperature. The quantitative analysis demonstrates that the predicted increase of the reduction probability of one state by a factor of 1.5 with respect to Born's rule can be measured by a few hundred statistically significant measurements.

Keywords: *Wavefunction collapse, Born's rule, superluminal signalling.*

1 Introduction

All models for wavefunction collapse have so far been unable to be checked by experiments. The gravity-based approaches of Diósi and Penrose [5, 6] or dynamical reduction models [7] require the measurement of the lifetimes of quantum superpositions, which e.g. can be carried out by measuring the vanishing of quantum interference between superposed states, such as in the famous mirror-experiment of Marshall [8]. However, such procedures are always disturbed by the unavoidable decoherence between the superposed states due to environmental interaction, whose suppression by e.g. very low temperatures or an ultra-high vacuum is difficult to arrange.

¹ My official last name is Wiese. For non-official concerns, my wife and I use our common family name: Quandt-Wiese.

A basically new perspective for checking a collapse model is provided by the recently published *Dynamical Spacetime approach* to wavefunction collapse [1, 2], which predicts, beside lifetimes of superpositions, new effects in the form of deviations from Born's rule for special regimes. The Dynamical Spacetime approach is as the approaches of Diósi and Penrose a gravity-based approach, which enhances semiclassical gravity by postulating that the spacetime region on which quantum fields exist and on which the wavefunction's evolution can be regarded is bounded towards the future by a spacelike hypersurface, which is dynamically expanding towards the future. Collapse is displayed in the way that the wavefunction's evolution becomes unstable at certain critical expansions of spacetime, at which it reconfigures via a self-reinforcing mechanism quasi-abruptly to a new evolution resembling a classical trajectory. In EPR experiments, this quasi-abrupt reconfiguration of the wavefunction's evolution can concern far-separated regions. The second important feature of the Dynamical Spacetime approach, which provides the perspective for an experimental check, is its capability to forecast reduction probabilities on the basis of a physical argument. This explains why all experiments performed so far behave in accordance with Born's rule, and predict deviations from it, when solids evolve into three-state superpositions. The Dynamical Spacetime approach is the first collapse model open to deviations from Born's rule, because it does not fear the consequences possibly resulting from superluminal signalling. The explanation of the "spooky action at a distance" by the quasi-abrupt reconfigurations of the wavefunction's evolution does not come in conflict with the principles of relativity [1, 2].

Since a measurement of reduction probabilities for proving deviations from Born's rule is not disturbed by state decoherence, one does not have to arrange special experimental conditions, such as low temperatures or an ultra-high vacuum, for suppressing it to a minimum. This provides a realistic perspective for checking the Dynamical Spacetime approach; the experiments can even be performed at room temperature!

The challenge for checking the Dynamical Spacetime approach follows from the fact that the deviations from Born's rule for solids in three-state superpositions occur only when the displacements between the states are at the reduction point in time, significantly larger than the spatial variation of the solid's nuclei. To ensure this condition, the reduction point time of the setup has to be forecasted as precisely as possible. This is effected with the help of a formulary for the Diósi-Penrose criterion for solids in quantum superpositions, which is developed in a separate publication [3], but whose study is not essential here. Furthermore, interactions of the setup with the environment during superposition have to be suppressed to a minimum, since such interactions influence the reduction point in time. Therefore, the setup during superposition is not in contact with the measuring devices. The experiment's result is determined a sufficient time after reduction, by e.g. connecting a voltmeter with the setup.

The remainder of paper is structured as follows. In Sections 2 and 3, the Dynamical Spacetime approach and the underlying mathematical model are discussed. In Sections 4 and 5, the setup is introduced, and the experiment's feasibility is demonstrated by a detailed quantitative analysis. In Section 6, an outlook on pursuing experiments is given.

2 Dynamical Spacetime approach

In this and the following section, we give a brief overview of the Dynamical Spacetime approach to wavefunction collapse and its mathematical model. For starting with the Dynamical Spacetime approach, the overview article [1] is recommended. The mathematical model is derived in [2].

1. Physical approach

The Dynamical Spacetime approach is based on two assumptions: semiclassical gravity and the so-called *Dynamical Spacetime postulate*.

Semiclassical gravity: In semiclassical gravity, the gravitational field is not quantised and spacetime geometry is treated classically [9, 10]². As a consequence, superposed states must share the same classical spacetime geometry, even if they prefer (according to general relativity) differently curved spacetimes, which is the case when their mass distributions are different. This provokes a competition between the states for the curvature of spacetime, which is the driver of collapse in the Dynamical Spacetime approach. However, semiclassical gravity alone cannot explain collapse, which is known from studies of the Schrödinger-Newton equation to display semiclassical gravity in the Newtonian limit [11, 12].

Dynamical Spacetime postulate: The Dynamical Spacetime approach postulates that the spacetime region on which quantum fields exist and on which the wavefunction's evolution can be regarded is bounded towards the future by a spacelike hypersurface, the so-called *spacetime border* $\bar{\sigma}$, which is dynamically propagating towards the future over the so-called *dynamical parameter* $\bar{\tau}$. The dynamical parameter itself is not an observable quantity (beable), and can be chosen to be dimensionless. This postulate enables a fundamentally new behaviour in the way that the wavefunction's evolution on spacetime can retroactively change to a new evolution, when spacetime expands over $\bar{\tau}$. This is possible, since the wavefunction's evolution is not governed by the unitary evolution only, but must in addition satisfy a boundary condition on the spacetime border.

2. Collapse mechanism

The most important result of the Dynamical Spacetime approach is that it leads to a physical mechanism for collapse. Collapse is displayed in the way that the wavefunction's evolution becomes unstable at certain critical positions of the spacetime border; the so-called *reduction positions* $\bar{\sigma}(\bar{\tau}_C)$. At these positions, the wavefunction's evolution reconfigures via a self-reinforcing mechanism quasi-abruptly to a new evolution, which then resembles a classical trajectory. Thereby, spacetime geometry changes in favour of the winning state, which causes the path of the other (competing) state

² The question of whether the gravitational field must be quantised is still the subject of scientific debate [13, 14], and an issue that has not yet been determined by experiments [15].

to vanish by simple destructive interference. The lifetimes of superpositions following from this mechanism are identical to those resulting from the gravity-based approaches of Diósi and Penrose [5, 6].

The abrupt reconfigurations of the wavefunction's evolution, which can cover far-distant spacetime regions and which always incorporate the complete history of the superposition (which begins when a wavepacket in configuration space has split), can explain the quantum correlations in EPR experiments, even of such with free choice of measurements. Here Bob can instantaneously influence, by the orientation of his polarisation filter, the polarisation of the photon on Alice's side via the abrupt reconfigurations of the wavefunction's evolution. Although this is a faster-than-light mechanism for the explanation of the "spooky action at a distance", it does not provoke a conflict with relativity, since causality does not evolve along free selectable Lorentz frames in spacetime in the Dynamical Spacetime approach, but is parametrised by the expansion of spacetime (i.e. by the dynamical parameter $\bar{\tau}$) and evolves quasi-orthogonal to it.

3. Reduction probabilities

The second important result of the Dynamical Spacetime approach is its capability to forecast reduction probabilities on basis of a physical argument. The probabilities with which the wavefunction's evolution reconfigures at the reduction positions to one state of the superposition depend on how frequently the intensities of the states fluctuate for decay. This can be expressed in terms of so-called *decay-trigger rates* of the states, which depend on the energy increases the states suffer due to the sharing of spacetime geometry in semiclassical gravity. In the Newtonian limit, these energy increases follow from the fact that the states do not reside in their own gravitational potential (resulting from their mass distributions) but in the mean gravitational potential of the superposed states. For two-state superpositions, this leads to energy increases of the states that are proportional to the intensity of the respective competing state to which the state will decay, and therefore to reduction probabilities being proportional to the state's intensity, i.e. to Born's rule. This derivation of Born's rule for two-state superpositions can be adapted to all experiments conducted so far with the help of a property that these experiments have in common: they lead to never more than two different mass distributions at one location. These mass distributions refer e.g. to the cases that a particle "is", or "is not", detected at the location.

4. Deviations from Born's rule for solids in three-state superpositions

The Dynamical Spacetime approach predicts deviations from Born's rule when solids evolve into three-state superpositions. Such a superposition can be created by splitting a photon into three beams and measuring it by detectors, which displace a solid at different distances for photon detection, as shown in Figure 1. When the displacement Δ_{s_1} between the solid in State 0 and State 1 is, at the reduction position, much larger than the spatial variation of its nuclei σ_n , so that the mass distributions of States 0 and 1 are disjoint (cf. Figure 1), and when the displacement between States 2 and 0 is much

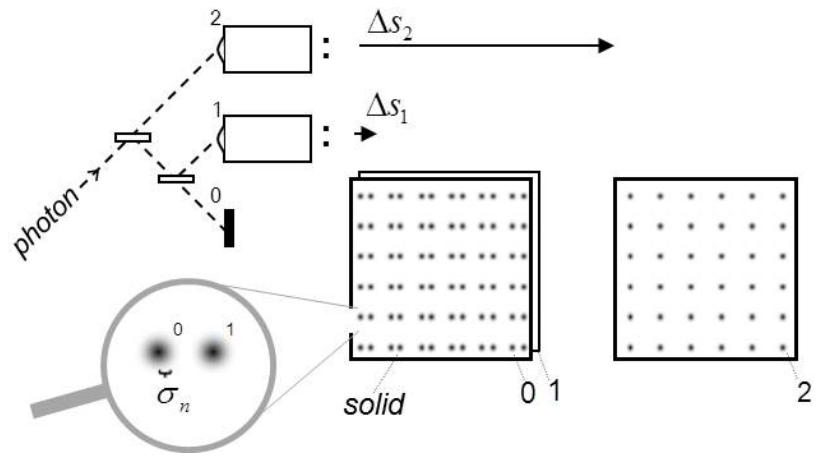


Fig. 1: Experiment to transfer a solid into a three-state superposition. For photon detection, Detectors 1 and 2 displace the solid by Δs_1 , respectively Δs_2 .

larger than that between States 1 and 0 ($\Delta s_2 \gg \Delta s_1$), the reduction probability of State 2 increases with respect to Born's rule. Disjoint mass distributions are the criterion that the decay-trigger rates of States 1 and 2 are decorrelated. Then, they both trigger a reconfiguration of the superposition in favour of State 2, which increases the reduction probability of this state with respect to Born's rule.

3 Mathematical model

In this section, we recapitulate the mathematical model of the Dynamical Spacetime approach, which is derived in [2]. We focus on what is needed for the discussion of the later experiments and limit ourselves to the Newtonian limit. In Section 3.1, we discuss the basic concepts of the Dynamical Spacetime approach, the so-called *classical scenarios* and *competition actions*, with which we formulate the mathematical model in Section 3.2. In Section 3.3, we present the most important formulae of the formulary for the Diósi-Penrose criterion for solids in quantum superpositions developed in [3], which is needed for the quantitative analysis of the experiments. In Section 3.4, we apply the model to the experiment in Figure 1, and derive first results for the later discussion.

3.1 Classical scenarios and competition actions

In this section, we show how the wavefunction's evolution can be decomposed into so-called *classical scenarios*, with which we can conveniently describe the abrupt reconfigurations of the wavefunction's evolution at the critical positions of spacetime border. Furthermore, we introduce the so-called *competition actions*, with which we can measure how much the preferred spacetime geometries of the classical scenarios differ, and how strongly they compete for spacetime geometry.

Aligning spacetime border's propagation with the experiment's rest frame

Most predictions of the Dynamical Spacetime approach are fortunately not sensitive to the concrete propagation of the spacetime border $\bar{\sigma}(\bar{\tau})$. The discussion of the experiments in this paper can be simplified by assuming that the spacetime border propagates in coincidence with the experiment's rest frame. The spacetime border is then given by a plane hypersurface, which is specified by a point in time \bar{t} in this rest frame; and the dynamical parameter $\bar{\tau}$ can be expressed by this point in time \bar{t} (i.e. $\bar{\tau} \rightarrow \bar{t}$). This is very convenient for analyses, since spacetime then simply ends at \bar{t} . Accordingly, the reduction positions of spacetime border $\bar{\tau}_C$ can be expressed by the corresponding *reduction points in time* \bar{t}_C .

Classical scenarios

Using the convention of classical scenarios, the state vector's evolution $|\psi(t)\rangle$ is decomposed into evolutions $|\tilde{\psi}_i(t)\rangle$ resembling approximately classical trajectories of the system, the *classical scenarios*, as:

$$|\psi(t)\rangle = \sum_i c_i |\tilde{\psi}_i(t)\rangle, \quad (1)$$

with $\langle \tilde{\psi}_i(t) | \tilde{\psi}_i(t) \rangle = 1$ and $\sum_i |c_i|^2 = 1$. In our discussion, the state vector $|\psi\rangle$ will always

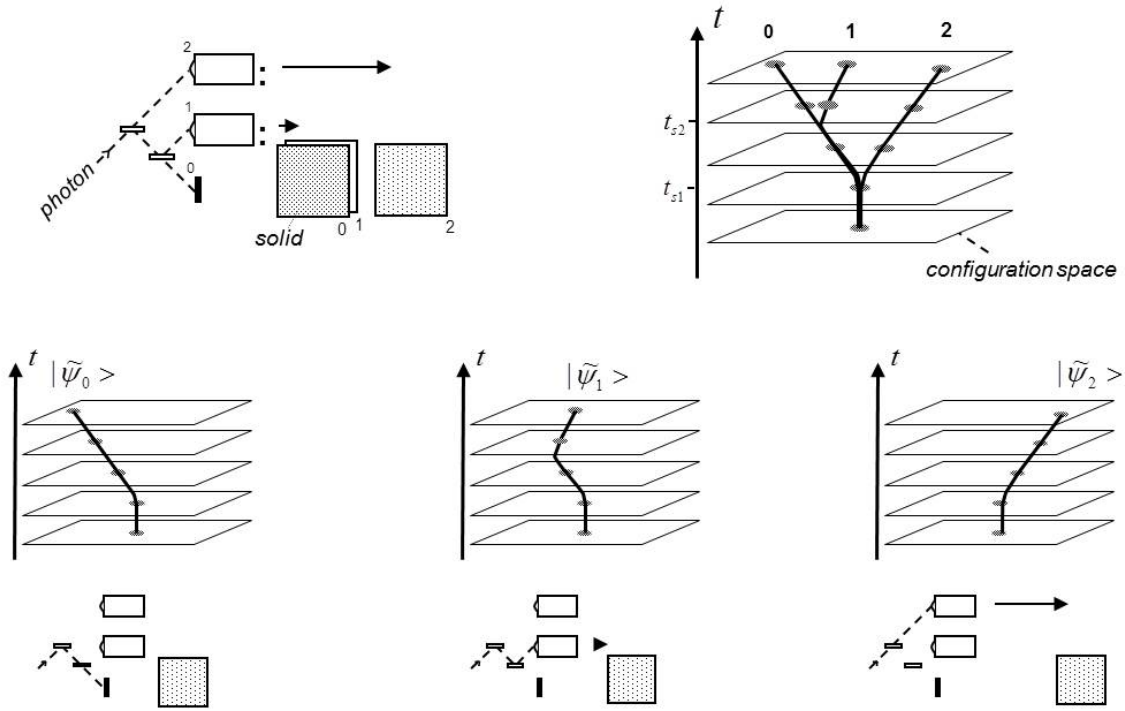


Fig. 2: Three classical scenarios $|\tilde{\psi}_0(t)\rangle$, $|\tilde{\psi}_1(t)\rangle$ and $|\tilde{\psi}_2(t)\rangle$ (middle part) of the experiment in Figure 1 (upper left), which are defined by following up state vector's evolution $|\psi(t)\rangle$ on classical paths in configuration space (upper right), and for which the system evolves on classical trajectories in spacetime, as illustrated at the bottom.

describe the complete system, consisting of the experiment in Figure 1 of the photon, the beam splitters, the detectors and the solid. The upper right part of Figure 2 illustrates state vector's evolution $|\psi(t)\rangle$ in configuration space of this experiment, which consists at the beginning of one wavepacket splitting into separate ones when the photon enters a beam splitter. The middle part in Figure 2 shows the three classical scenarios $|\tilde{\psi}_0(t)\rangle$, $|\tilde{\psi}_1(t)\rangle$ and $|\tilde{\psi}_2(t)\rangle$ of the experiment, which are defined by following up the state vector's evolution on classical paths in configuration space, and for which the system evolves on classical trajectories in spacetime. For e.g. Classical Scenario 2 $|\tilde{\psi}_2(t)\rangle$, the photon is completely transmitted at the first beam splitter, and is only detected by Detector 2 displacing the solid by Δs_2 , as illustrated in the lower right of Figure 2. The classical scenarios are not solutions of Schrödinger's equation at the points in time t , at which the state vector $|\psi(t)\rangle$ splits into two wavepackets in configuration space, when the photon enters a beam splitter. To fulfil the decomposition of the state vector's evolution according to Equation (1) in the regions where several classical scenarios refer to the same root wavepacket, their phases must be chosen suitably. For e.g. the common root wavepacket of all classical scenarios, their phases must satisfy $|\sum_i |c_i| e^{i\varphi_i}| = 1$.

The concept of classical scenarios is very important for the Dynamical Spacetime approach, since the abrupt reconfigurations of the wavefunction's evolution at collapse can simply be described by intensity shifts between the scenarios. In the Dynamical Spacetime approach, the intensity of a path in configuration space, such as e.g. the

path of State 2 between t_{s1} and \bar{t} in Figure 2, drops when the spacetime geometry changes to the disadvantage of this path. This enforces, due to the norm conservation of unitary evolution, that at the wavepacket's splitting point at t_{s1} more intensity is rerouted to the other path belonging to States 0 and 1. This rerouting of intensity at t_{s1} can be expressed by shifting intensity from Classical Scenario 2 to the Scenarios 0 and 1. Thus, the reconfigurations of the wavefunction's evolution can be described by intensity shifts between the classical scenarios³.

In the following discussion, we abbreviate the intensities $|c_i|^2$ of the classical scenarios by

$$I_i \equiv |c_i|^2 \quad . \quad \text{intensities of classical scenarios} \quad (2)$$

Diósi-Penrose energies and competition actions

In this section, we present the so-called *Diósi-Penrose energies*, which define a measure of how much the preferred spacetime geometries of two states differ from each other. They coincide with the characteristic gravitational energy resulting from the gravity-based collapse models of Diósi and Penrose [4].

How much the preferred spacetime geometries of two states differ on an area A , which we call the *bundle area*, can be measured with the help of the so-called *local Diósi-Penrose energies*, which depend on how much the mass distributions of the states differ from each other on A . For the discussion of the experiment in Figure 1, we regard for the local Diósi-Penrose energies the area of the solid ($A=S$) and the areas of the two detectors ($A=D1, D2$). For the discussion of the concrete experiments in Section 5, we take into account that not only the solid on $A=S$ has different mass distributions in its states, but that also the two detectors have slightly different mass distributions in their detection and no-detection states. On the bundle area of Detector 2 ($A=D2$), States 0 and 1, both referring to the no-detection case of this detector, have identical mass distributions, which we combine to a so-called *local bundle* on this area. Accordingly, States 0 and 2 are a local bundle on the area of Detector 1 ($A=D1$). The local Diósi-Penrose energies $E_{G\kappa\nu}^A$ are defined between two of such local bundles (κ and ν) on A , where a local bundle can also be a single state. The Diósi-Penrose energy is given by the integral over the difference of the bundles' mass distributions $\rho_\kappa(\mathbf{x}) - \rho_\nu(\mathbf{x})$ multiplied by the difference of their gravitational potentials $\Phi_\kappa(\mathbf{x}) - \Phi_\nu(\mathbf{x})$ resulting from the mass distributions⁴. On the bundle areas of Detector 1 and 2, we can define respectively one local Diósi-Penrose energy E_G^{D1} and E_G^{D2} between the two bundles referring to the detection and no-detection cases of the detector as follows [4]:

³ The intensity shifts between classical scenarios must be accompanied by readjustments of their phases φ_i in the regions where they refer to common root wavepackets to satisfy Equation (1) after reconfiguration.

⁴I.e. $\Phi_\kappa(\mathbf{x}) = -G \int d^3\mathbf{y} \rho_\kappa(\mathbf{y}) / |\mathbf{x} - \mathbf{y}|$.

$$E_G^{Di} = \frac{1}{2} \int_{\mathbf{x} \in Di} d^3\mathbf{x} (\rho_{det}(\mathbf{x}) - \rho_{no-det}(\mathbf{x})) (\Phi_{no-det}(\mathbf{x}) - \Phi_{det}(\mathbf{x})) . \quad (3)$$

Diósi-Penrose energies of the detectors

Accordingly, we obtain three local Diósi-Penrose energies between States 0, 1 and 2 on the bundle area of the solid ($E_{G01}^S, E_{G02}^S, E_{G12}^S$), which are given by

$$E_{Gij}^S = \frac{1}{2} \int_{\mathbf{x} \in S} d^3\mathbf{x} (\rho_i(\mathbf{x}) - \rho_j(\mathbf{x})) (\Phi_j(\mathbf{x}) - \Phi_i(\mathbf{x})) . \quad (4)$$

Diósi-Penrose energies of the solid

How much the preferred spacetime geometries of two local bundles of classical scenarios κ and ν differ on the spacetime region, which is given by the area A , and limited towards the future by the spacetime border at \bar{t} , is measured by the so-called *local competition actions* $S_{G\kappa\nu}^A(\bar{t})$. They are defined by integrating the local Diósi-Penrose energies between the corresponding bundles of states over time until the spacetime border at \bar{t} ($S_{G\kappa\nu}^A(\bar{t}) = \int_{..}^{\bar{t}} dt E_{G\kappa\nu}^A(t)$). The local competition actions between the detection and no-detection cases of the detectors ($S_G^{D1}(\bar{t}), S_G^{D2}(\bar{t})$) are given by

$$S_G^{Di}(\bar{t}) = \int_{..}^{\bar{t}} dt E_G^{Di}(t) , \quad \text{competition actions of the detectors} \quad (5)$$

and the local competition actions between the three states on the bundle area of the solid ($S_{G01}^S(\bar{t}), S_{G02}^S(\bar{t}), S_{G12}^S(\bar{t})$) by

$$S_{Gij}^S(\bar{t}) = \int_{..}^{\bar{t}} dt E_{Gij}^S(t) . \quad \text{competition actions of the solid} \quad (6)$$

3.2 Reconfiguration equation and rule

In this section, we present the mathematical model of the Dynamical Spacetime approach, which describes when, how and with which probabilities the wavefunction's evolution reconfigures.

Reconfiguration equation

The so-called *reconfiguration equation* is a conditional equation that depends on the intensities of the classical scenarios I_i and the local competition actions $S_{G\kappa\nu}^A(\bar{t})$ between them, and whose solutions determine whether intensity changes of the classical scenarios dI_i are possible. It is given by the following set of equations (one equation for every state i) [2]:

$$dI_i = \sum_{A; \kappa \supseteq i} \frac{dI_i}{dI_\kappa} \sum_{\nu \neq \kappa} \frac{S_{G\kappa\nu}^A(\bar{t})}{\hbar} (I_\nu dI_\kappa - I_\kappa dI_\nu) . \quad \text{reconfiguration equation} \quad (7)$$

Here the outer sum runs over all bundle areas A , on which local competition actions $S_{G\kappa\nu}^A(\bar{t})$ can be defined. The condition $\kappa \supseteq i$ selects for an area A the local bundle κ , which contains the regarded state i . The inner sum runs over all other local bundles ν on A competing with κ for spacetime geometry. I_κ and I_ν are the intensities and dI_κ , dI_ν the intensity changes of the local bundles κ and ν , where the intensity of a local bundle is given by the sum of the intensities of its states ($I_\kappa = \sum_{i \in \kappa} I_i$).

The reduction point in time \bar{t}_C of a superposition of classical scenarios is given by the lowest value of \bar{t} for which the reconfiguration equation has non-vanishing solutions for the intensity changes dI_i .

For our experiment in Figure 1, the reconfiguration equation is given by⁵

$$\begin{pmatrix} dI_0 \\ dI_1 \\ dI_2 \end{pmatrix} = \frac{1}{\hbar} \left[\begin{pmatrix} S_{G01}^S I_1 + S_{G02}^S I_2 & -S_{G01}^S I_0 & -S_{G02}^S I_0 \\ -S_{G01}^S I_1 & S_{G01}^S I_0 + S_{G12}^S I_2 & -S_{G12}^S I_1 \\ -S_{G02}^S I_2 & -S_{G12}^S I_2 & S_{G02}^S I_0 + S_{G12}^S I_1 \end{pmatrix} + (S_G^{D1} + S_G^{D2}) \begin{pmatrix} 1 & 0 & 0 \\ 0 & 1 & 0 \\ 0 & 0 & 1 \end{pmatrix} \right] \begin{pmatrix} dI_0 \\ dI_1 \\ dI_2 \end{pmatrix} . \quad (8)$$

The reduction point in time \bar{t}_C follows by determining the point in time \bar{t} for which the largest eigenvalue e_{max} of the matrix inside the square bracket reaches Planck's quantum of action, i.e. $e_{max}(\bar{t}_C) = \hbar$. The corresponding eigenvector $d\vec{I} \equiv (dI_0, dI_1, dI_2)^T$ is called the *reconfiguration solution* $d\vec{I}_C$. The intensity vectors of the classical scenarios $\vec{I} \equiv (I_0, I_1, I_2)^T$ after reconfiguration of the wavefunction's evolution at collapse are either $\vec{I}'_+ = \vec{I} + \hat{\alpha}_+ d\vec{I}_C$ or $\vec{I}'_- = \vec{I} - \hat{\alpha}_- d\vec{I}_C$, where $\hat{\alpha}_+$ and $\hat{\alpha}_-$ are the largest numbers for which $\vec{I} + \hat{\alpha}_+ d\vec{I}_C$ respectively $\vec{I} - \hat{\alpha}_- d\vec{I}_C$ have no negative components [2]. In favour of which final state (\vec{I}'_+ or \vec{I}'_-) the wavefunction's evolution reconfigures at \bar{t}_C depends on smallest intensity fluctuations, which can be described with the so-called *decay-trigger rates* of the local bundles.

Decay-trigger rates

In semiclassical gravity, the energy of a local bundle on a bundle area A increases due to the sharing of spacetime geometry with the other competing bundles ν on A [4]. These energy increases divided by Planck's constant \hbar determine the decay-trigger rates $dp_{\kappa\downarrow}/d\bar{t}$ of the local bundles, which describe the probability $dp_{\kappa\downarrow}$ for an intensity fluctuation for decay (i.e. the probability for a decay-trigger) during spacetime border

⁵The term $dI_1/dI_{det} S_G^{D1}(\bar{t})(I_{no-det} dI_{det} - I_{det} dI_{no-det})$ occurring for the area of Detector 1 ($A=D1$) is transformed with $I_{det} + I_{no-det} = 1$ and $dI_{det} + dI_{no-det} = 0$ to $dI_1 S_G^{D1}(\bar{t})$, and the terms $dI_i/dI_{no-det} S_G^{D1}(\bar{t})(I_{det} dI_{no-det} - I_{no-det} dI_{det})$ with $i=0, 2$ to $dI_i S_G^{D1}(\bar{t})$. The terms corresponding to Detector 2 are transformed accordingly.

moving by $d\vec{t}$ [2]. The energy increase $E_{G\kappa}$ of a local bundle κ depends on the intensities I_ν of the competing bundles ν on A multiplied by the Diósi-Penrose energies $E_{G\kappa\nu}^A$ between them, i.e. $E_{G\kappa} = \sum_{\nu \neq \kappa} I_\nu E_{G\kappa\nu}^A$ [4]. The decay-trigger rates of the three local bundles on the area of the solid, which are identical to States 0, 1 and 2, are given by

$$\begin{aligned} \frac{dp_{0\downarrow}}{d\vec{t}} &= \frac{1}{\hbar} (I_1 E_{G01}^S + I_2 E_{G02}^S) \\ \frac{dp_{1\downarrow}}{d\vec{t}} &= \frac{1}{\hbar} (I_0 E_{G01}^S + I_2 E_{G12}^S) \\ \frac{dp_{2\downarrow}}{d\vec{t}} &= \frac{1}{\hbar} (I_0 E_{G02}^S + I_1 E_{G12}^S) \end{aligned} \quad \cdot \quad \text{decay-trigger rates of states} \quad (9)$$

Since the two detectors in the experiment in Figure 1 will be designed in such a way that their Diósi-Penrose energies are much smaller than those of the solid ($E_G^{Di} \ll E_{Gi}^S$; see Section 5.3), we do not present here the decay-trigger rates of the detectors $dp_{det\downarrow}^{Di}/d\vec{t}$ and $dp_{no-det\downarrow}^{Di}/d\vec{t}$ referring to the detection and no-detection bundles on $A=D1, D2$. Their impact on the final reduction probabilities can be easily determined with the results derived in [2].

Reconfiguration rule

In favour of which final state, $\vec{I}'_+ = \vec{I} + \hat{\alpha}_+ d\vec{I}_C$ or $\vec{I}'_- = \vec{I} - \hat{\alpha}_- d\vec{I}_C$, the decay-trigger rates of States 0, 1 and 2 trigger the reconfiguration process depend on the projection of these states on the reconfiguration solution $d\vec{I}_C$, which is given by dI_{Ci} [2]. For $dI_{Ci} < 0$, a decay-trigger of state i triggers a reconfiguration to $\vec{I}'_+ = \vec{I} + \hat{\alpha}_+ d\vec{I}_C$, and for $dI_{Ci} > 0$ to $\vec{I}'_- = \vec{I} - \hat{\alpha}_- d\vec{I}_C$. This can be summarised by the following so-called *reconfiguration rule*⁶ [2]:

$$\vec{I} \rightarrow \begin{cases} \vec{I}'_+ = \vec{I} + \hat{\alpha}_+ d\vec{I}_C & \text{with } p_+ \propto \sum_i \Theta_0(-dI_{Ci}) \frac{dp_{i\downarrow}}{d\vec{t}} \\ \vec{I}'_- = \vec{I} - \hat{\alpha}_- d\vec{I}_C & \text{with } p_- \propto \sum_i \Theta_0(dI_{Ci}) \frac{dp_{i\downarrow}}{d\vec{t}} \end{cases}, \quad \text{reconfiguration rule} \quad (10)$$

which describes the possible reconfigurations of the intensity vector \vec{I} and the relative probabilities p_+ and p_- of these reconfigurations. The absolute reconfiguration probabilities follow by normalisation, i.e. by $p_+ + p_- = 1$.

Decorrelation criterion

When the displacement between two states becomes very small, such as e.g. between States 0 and 1 in Figure 1 for $\Delta s_1 \rightarrow 0$, their decay-trigger rates are correlated, and

⁶ $\Theta_0(x) = 0$ for $x \leq 0$, $\Theta_0(x) = 1$ for $x > 0$.

cannot be counted twice in the reconfiguration rule. The decay-trigger rates of two states are decorrelated when their mass distributions are disjoint [2]. For States 0 and 1 in Figure 1, this is given when the displacement between the states Δ_{s_1} is at least six times larger than the spatial variation σ_n of the solid's nuclei⁷ (cf. inset in Figure 1). The spatial variation σ_n of a solid's nuclei is typically on the order of a tenth of an Ångström [3]. This leads to the following so-called *decorrelation criterion*:

$$\Delta_{s_1}(\bar{t}_C) > 6\sigma_n \quad , \quad \text{decorrelation criterion} \quad (11)$$

which has to be fulfilled at the reduction point in time \bar{t}_C [2].

3.3 Diósi-Penrose energies of superposed solids

In this section, we present the most important formulae of the formulary for the Diósi-Penrose criterion for solids in quantum superpositions developed in [3], which we need for the quantitative analysis in Section 5.

The solid that will evolve into a three-state superposition with the setup proposed in Section 4 is a capacitor with a piezo as dielectric, which we call the *piezo capacitor*. The capacitor's plates are pressed apart from each other by the converse piezo electric effect when it is charged. In [3], we developed the basic formulae, with which we could calculate the Diósi-Penrose energy of such a piezo capacitor in a quantum superposition. The contribution of the capacitor's plates is calculated with a formula developed for a *displaced plate*, which is displaced by Δ_s vertically to its surface in one state of the superposition. The contribution of the piezo is calculated with a formula developed for an *extended plate*, whose thickness d is changed by Δd in one state of the superposition.

For displacements much larger than the mean lattice constant of the solid \bar{g} ($\Delta_s \gg \bar{g}$), which is typically in the order of two Ångströms ($\bar{g} \approx 2\text{Å}$), the solid can be approximated by a continuum [3]. The Diósi-Penrose energy resulting from this approximation is called the *long-distance contribution* to the Diósi-Penrose energy. For smaller displacements, the microscopic mass distribution of the solid's nuclei must be taken into account, which leads to a further contribution: the so-called *short-distance contribution* to the Diósi-Penrose energy. The Diósi-Penrose energies of the displaced and extended plate are given by

$$E_G^S(\Delta_s) = 2\pi\alpha_{geo}GV\rho^2\Delta_s^2 + E_G^{Ss}(\Delta_s) \quad , \quad (12)$$

where the first term describes the long-distance and $E_G^{Ss}(\Delta_s)$ the short distance contribution to the Diósi-Penrose energy. In this result, G is the gravitational constant, ρ the

⁷The mass distributions of the solid's nuclei can be described by Gaussian distributions, i.e. by $\rho(\mathbf{x}) \propto \exp(-\mathbf{x}^2/(2\sigma_n^2))$ [3].

mass density of the solid, V the volume of the plate and α_{geo} the so-called *geometric factor*, which is 1 for the displaced and $\frac{1}{3}$ for the extended plate. For the extended plate, Δ_s describes the displacement of the plate's surface, i.e. $\Delta_s = \Delta d/2$. The term $E_G^{Ss}(\Delta_s)$ for the short-distance contribution is given by

$$E_G^{Ss}(\Delta_s) = \bar{T}_G^S V \cdot \begin{cases} \frac{\alpha_{geo}}{12} \left(\frac{\Delta_s}{\sigma_n}\right)^2 & \Delta_s \ll \sigma_n \\ F_{geo}\left(\frac{\Delta_s}{\sigma_n}\right) & \Delta_s > 4\sigma_n \end{cases}, \quad (13)$$

where \bar{T}_G^S is the so-called *characteristic Diósi-Penrose energy density of a solid*⁸, σ_n the spatial variation of the solid's nuclei and $F_{geo}(x)$ the so-called *geometric function*⁹, which converges for $x \gg 1$ to one. The characteristic Diósi-Penrose energy density of a solid divided by Planck's constant \bar{T}_G^S/\hbar ranges from $4MHz/cm^3$ for aluminium, to over $42MHz/cm^3$ for iron, and up to $730MHz/cm^3$ for iridium [3]. The spatial variation σ_n of a solid's nuclei at room temperature is typically on the order of one-tenth of an Ångström ($\sigma_n \approx 0.1\text{Å}^{10}$). For displacements much larger than the nuclei's spatial variation ($\Delta_s \gg \sigma_n$), the short-distance contribution to the Diósi-Penrose energy converges to a constant value, which is given by $\bar{T}_G^S V$. This contribution can be neglected in Equation (12) for displacements much larger than the solid's mean lattice constant ($\Delta_s \gg \bar{g}$).

3.4 Application

In this section, we apply the mathematical model of the Dynamical Spacetime approach to the experiment in Figure 1. We derive results that we can use for the quantitative

⁸The characteristic Diósi-Penrose energy density of a solid is given by

$$\bar{T}_G^S/\hbar = \frac{G\hat{q}\rho^2\bar{g}^3}{\sqrt{\pi}\sigma_n},$$

where \hat{q} is the so-called *quadratic mass factor*, which is one for solids consisting of only one chemical element [3].

⁹The geometric functions of the displaced and extended plate are given by [3]

$$F_{d-pl}(x) = 1 - \frac{\sqrt{\pi}}{x},$$

$$F_{e-pl}(x) = 1 - \frac{2 + \sqrt{\pi}/2 - \sqrt{\pi}\ln(4)}{x} - \sqrt{\pi}\frac{\ln(x)}{x}.$$

¹⁰At room temperature, the spatial variation of the nuclei is mainly determined by the excited acoustical phonons, and can be estimated with the solid's Debye temperature Θ_D by [3]

$$\sigma_n = \sqrt{\frac{3T}{k_B \bar{m}} \frac{\hbar}{\Theta_D}},$$

where k_B is Boltzmann's constant, T the temperature and \bar{m} the mean mass of the solid's nuclei.

discussion of the real experiments in Section 5.

Impact of the detectors

The impact of the two detectors in Figure 1 on the reduction point in time \bar{t}_C can be discussed with Equation (8). When e_{max}^S is the largest eigenvalue of the left matrix in Equation (8) corresponding to the solid, \bar{t}_C is given by

$$e_{max}^S(\bar{t}_C) + S_G^{D1}(\bar{t}_C) + S_G^{D2}(\bar{t}_C) = \hbar . \quad \text{reduction condition} \quad (14)$$

This result shows that the competition actions of the detectors S_G^{D1} and S_G^{D2} shorten the reduction point in time \bar{t}_C . Too great competition actions of the detectors can therefore prevent the displacement between States 0 and 1 at the reduction point not being sufficiently large to satisfy the decorrelation criterion $\Delta s_1(\bar{t}_C) > 6\sigma_n$. In Section 5.3, we show that the detectors can be designed in such a way that their Diósi-Penrose energies are much smaller than those of the solid ($E_G^{Di} \ll E_{Gij}^S$), which allows us to neglect their impact on the reduction point in time. In the following discussion, the competition actions of the detectors are therefore no longer considered.

Procedure for calculating \bar{t}_C and p_2

In this section, we describe the general procedure for calculating the reduction point in time \bar{t}_C and the reduction probability of State 2 p_2 of the experiment in Figure 1. This procedure is used for the exact numerical calculations of the experimental proposal in Section 5. When we know the time profiles of the displacements between the states in Figure 1 $\Delta s_i(t)$, we can determine the Diósi-Penrose energies of the solid $E_{Gij}^S(t)$ with Equation (12), and the corresponding competition actions $S_{Gij}^S(\bar{t})$ with Equation (6). With the competition actions $S_{Gij}^S(\bar{t})$ and the intensity vector \vec{I} , we can then calculate the largest eigenvalue e_{max}^S of the left matrix in Equation (8) as a function of \bar{t} , and obtain the reduction point in time \bar{t}_C by

$$e_{max}^S(\bar{t}_C) = \hbar . \quad \text{reduction condition} \quad (15)$$

With the reconfiguration solution $d\vec{I}_C$, i.e. the eigenvector corresponding to e_{max}^S at \bar{t}_C , and the decay-trigger rates $dp_i/d\bar{t}$ of the states at the reduction point in time, which can be calculated with the corresponding Diósi-Penrose energies $E_{Gij}^S(\bar{t}_C)$ (Equation 9), we obtain with the reconfiguration rule (Equation 10) the final states $\vec{I}'_+ = \vec{I} + \hat{\alpha}_+ d\vec{I}_C$, $\vec{I}'_- = \vec{I} - \hat{\alpha}_- d\vec{I}_C$ and their reduction probabilities p_+ , p_- . In these final states, the experiment can still be in a two-state superposition. Such a two-state superposition will reduce at a later point in time, where the reduction probabilities follow Born's rule. The overall reduction probability for a reduction to State 2 p_2 is therefore given by

$$p_2 = p_+ I'_{+2} + p_- I'_{-2} . \quad (16)$$

Case " $\Delta s_2 \gg \Delta s_1$ "

In this section, we apply the procedure above to the case that the displacement between States 0 and 2 is much larger than that between States 0 and 1 ($\Delta s_2 \gg \Delta s_1$), as shown in Figure 1. The results of this limiting case can already be used for rough calculations of the real experiments, as will be shown in Section 5.

Since the Diósi-Penrose energies scale with the square of the displacement between the states (cf. Equation 12), the competition actions, which result from the Diósi-Penrose energies according to Equation (6), can be approximated for $\Delta s_2 \gg \Delta s_1$ by

$$\begin{aligned} S_{G02}^S(\bar{t}) &\approx S_{G12}^S(\bar{t}) \\ S_{G01}^S(\bar{t}) &\approx 0 \end{aligned} \quad . \quad (17)$$

With the reduction condition $e_{max}^S(\bar{t}_C) = \hbar$, follows then

$$S_{G02}^S(\bar{t}_C) = \hbar \quad . \quad \text{reduction condition} \quad (18)$$

When the displacements (and therefore also the Diósi-Penrose energies) between the states are constant over time, which means that the competition action is given by $S_{G02}^S(\bar{t}) = E_{G02}^S \bar{t}$, this reduction condition leads to $\bar{t}_C = \hbar / E_{G02}^S$. This reduction point in time \bar{t}_C coincides with the lifetimes of superpositions predicted by the gravity-based approaches of Diósi and Penrose [6, 16].

The reconfiguration solution $d\vec{I}_C$ corresponding to $e_{max}^S(\bar{t}_C)$ is (cf. Equation 8):

$$d\vec{I}_C = \begin{pmatrix} -I_0 \\ -I_1 \\ I_0 + I_1 \end{pmatrix} \quad . \quad (19)$$

This leads, with the reconfiguration rule (Equation 10), to the final states:

$$\vec{I}'_+ = \vec{I} + \hat{\alpha}_+ d\vec{I}_C = \begin{pmatrix} 0 \\ 0 \\ 1 \end{pmatrix} = \vec{I}_2 \quad , \quad \vec{I}'_- = \vec{I} - \hat{\alpha}_- d\vec{I}_C = \frac{1}{I_0 + I_1} \begin{pmatrix} I_0 \\ I_1 \\ 0 \end{pmatrix} = \vec{I}_{01} \quad , \quad (20)$$

where \vec{I}'_+ corresponds to State 2, which we abbreviated \vec{I}_2 , and \vec{I}'_- to a superposition of States 0 and 1, which we abbreviated \vec{I}_{01} . The decay-trigger rates of States 0 and 1 are both $I_2 \cdot E_{G12}^S / \hbar$, which follows with $E_{G02}^S \approx E_{G12}^S$, $E_{G01}^S \approx 0$ and Equation (9), and trigger according to the reconfiguration rule (Equation 10) a reconfiguration to \vec{I}_2 ($dI_{C0} < 0$, $dI_{C1} < 0$), when the decorrelation criterion $\Delta s_1(\bar{t}_C) > 6\sigma_n$ is satisfied. The decay-trigger rate of State 2 is $(I_0 + I_1) \cdot E_{G12}^S / \hbar$ and triggers a reconfiguration to \vec{I}_{01} ($dI_{C2} > 0$). This leads to $p_2 \propto 2I_2$, $p_{01} \propto (I_0 + I_1)$ and the following increased reduction probability of State 2 with respect to Born's rule ($p_2 = I_2$):

$$p_2 = \frac{2}{1 + I_2} I_2 \quad \text{for} \quad \Delta s_1(\bar{t}_C) > 6\sigma_n . \quad (21)$$

For $\Delta s_1=0$, when the decay-trigger rates of States 0 and 1 are correlated and account only once in the reconfiguration rule, we obtain $p_2 \propto I_2$, $p_{01} \propto (I_0 + I_1)$ and a reduction probability of State 2 in accordance with Born's rule:

$$p_2 = I_2 \quad \text{for} \quad \Delta s_1 = 0 . \quad (22)$$

Case " $\Delta s_2/\Delta s_1=4$ "

We now calculate a case that is already fairly close to the real experiments that will be discussed in Section 5. We regard the case that the displacement between States 0 and 2 is for all times t four times larger than that between States 0 and 1, i.e. $\Delta s_2(t)/\Delta s_1(t)=4$, and that the displacements are much larger than the solid's mean lattice constant ($\Delta s_i \gg \bar{g}$). The following calculations will show that the results do not differ much from the previous case " $\Delta s_2 \gg \Delta s_1$ ". This means that Equations (18) and (21) can be used for rough calculations of \bar{t}_C and p_2 of the real experiments.

According to Equations (12) and (13), the Diósi-Penrose energies between the three states E_{Gij}^S scale with the displacements between them, which are given by $\Delta s_i - \Delta s_j$ ¹¹, like $E_{Gij}^S(t) \propto (\Delta s_i - \Delta s_j)^2$, when the displacements are much larger than the solid's mean lattice constant ($\Delta s_i \gg \bar{g}$). When the displacement ratio $\Delta s_2/\Delta s_1$ is constant over time, the ratios between the Diósi-Penrose energies and the competition actions are given for all time t by the ratios between the squared displacements $(\Delta s_i - \Delta s_j)^2$ (e.g. $S_{G12}^S(\bar{t})/S_{G02}^S(\bar{t})=3^2/4^2$). This simplifies the calculation of the largest eigenvalue e_{max}^S of the left matrix in Equation (8) as a function of \bar{t} . For an intensity vector of $\vec{I}=(\frac{1}{2}, \frac{1}{4}, \frac{1}{4})^T$, the reduction condition $e_{max}^S(\bar{t}_C)=\hbar$ leads to

$$S_{G02}^S(\bar{t}_C) = 1.15\hbar , \quad \text{reduction condition} \quad (23)$$

which does not differ much from Equation (18) for " $\Delta s_2 \gg \Delta s_1$ ". The reconfiguration solution $d\vec{I}_C$ corresponding to $e_{max}^S(\bar{t}_C)$ is

$$d\vec{I}_C = \begin{pmatrix} -0.626 \\ -0.140 \\ 0.767 \end{pmatrix} . \quad (24)$$

With the reconfiguration rule (Equation 10), we obtain for $\Delta s_1(\bar{t}_C) > 6\sigma_n$ the following final states and corresponding reduction probabilities:

¹¹The displacement Δs_0 is defined by $\Delta s_0 \equiv 0$.

$$\vec{I}_+ = \vec{I} + \hat{\alpha}_+ d\vec{I}_C = \begin{pmatrix} 0 \\ 0.138 \\ 0.862 \end{pmatrix} \text{ with } p_+ = 0.406 \quad (25)$$

$$\vec{I}_- = \vec{I} - \hat{\alpha}_- d\vec{I}_C = \begin{pmatrix} 0.704 \\ 0.296 \\ 0 \end{pmatrix} \text{ with } p_- = 0.594$$

The overall reduction probability of State 2 follows with Equation (16) as $p_2=0.35$, which is by a factor of 1.40 larger than that expected by Born's rule ($p_2=I_2=\frac{1}{4}$). With Equation (21) for " $\Delta s_2 \gg \Delta s_1$ ", we obtain with $I_2 = \frac{1}{4}$ an increase of $p_2/I_2=1.6$ with respect to Born's rule, which does not differ much from $p_2/I_2=1.40$. The result of our calculation can be summarised by

$$S_{G02}^S(\bar{t}_C) = 1.15\hbar \quad p_2/I_2 = 1.40 \quad \text{for} \quad \begin{cases} \Delta s_2(t)/\Delta s_1(t) = 4 \\ \Delta s_2(\bar{t}_C) \gg \bar{g} \\ \Delta s_1(\bar{t}_C) > 6\sigma_n \\ \vec{I} = (\frac{1}{2}, \frac{1}{4}, \frac{1}{4})^T \end{cases} \quad (26)$$

4 Experiment

In this section, we present the experiment for checking deviations from Born's rule. In Section 4.1, we introduce the setup. In Section 4.2, we show how the interaction of the setup with the environment is minimised during superposition. In Section 4.3, we present the process of a measurement; and in Section 4.4, we summarise the technical parameters of the photodiodes that are needed for the quantitative analysis in Section 5.

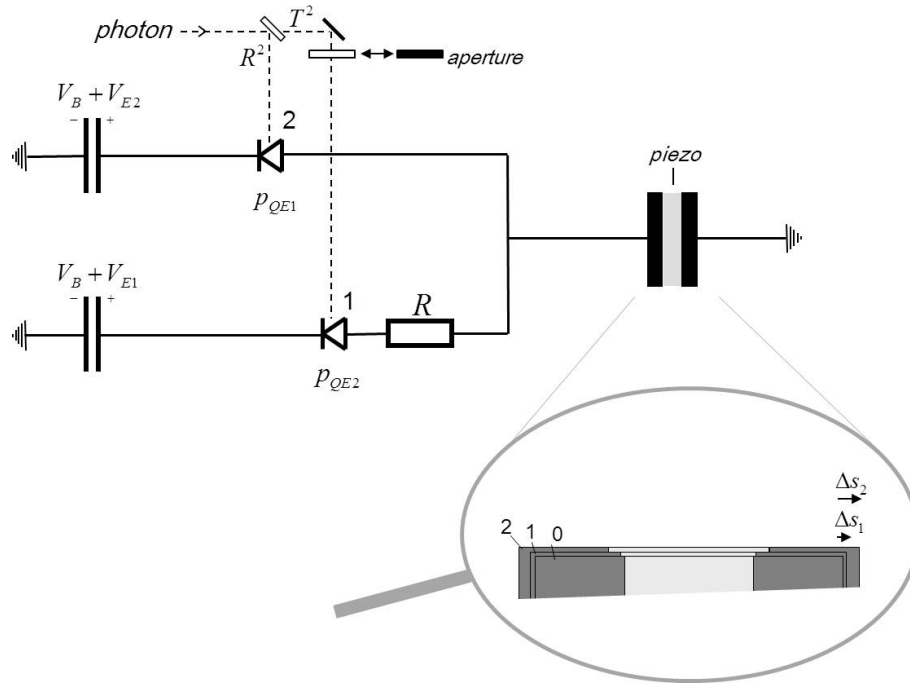


Fig. 3: Setup to allow the capacitor on the right to evolve into a three-state superposition, as illustrated in the inset.

4.1 Setup

Figure 3 shows the setup to allow solid to evolve into a three-state superposition. The solid that will evolve into this superposition is the capacitor at the right with the piezo as dielectric, which we call the *piezo capacitor*. The capacitor's plates are pressed apart from each other by the converse piezoelectric effect when it is charged, i.e. the piezo capacitor is working like a piezoactuator. The piezo capacitor is transferred into a three-state superposition by splitting the photon with the beam splitter into two beams and by measuring it with the two avalanche photodiodes in Figure 3, whose avalanche currents charge the capacitor with different strength, and which let the capacitor's plates be displaced by displacements of Δs_2 in State 2, and Δs_1 in State 1, as shown in the inset. The displacements Δs_1 and Δs_2 can be controlled by the photodiode's excess bias voltages V_{E1} and V_{E2} , and the resistor R behind Photodiode 1. The third state, i.e. State 0, in which the capacitor's plates are not displaced at all, occurs due to the

finite detection probabilities of the photodiodes (being smaller than one) automatically, which are called the photodiodes' *quantum efficiencies* p_{QE1} and p_{QE2} . The intensities of States 0, 1 and 2 of the so-generated three-state superposition depend on the photodiode's quantum efficiencies p_{QE1} and p_{QE2} , and the transmission coefficient T^2 and reflection coefficient R^2 of the beam splitter ($T^2 + R^2 \approx 1$) as follows:

$$\begin{aligned} I_0 &= 1 - T^2 p_{QE1} - R^2 p_{QE2} \\ I_1 &= T^2 p_{QE1} \\ I_2 &= R^2 p_{QE2} \end{aligned} \quad (27)$$

Quantum mechanical origin of quantum efficiencies

We assume that the photodiodes' finite quantum efficiencies ($p_{QE1}, p_{QE2} < 1$) have a quantum mechanical origin. This means that the photodiodes evolve after the photon's arrival into a superposition of a detection and no-detection state, reducing to one of these states after some time. If the photodiodes' finite quantum efficiencies would have a classical origin, such as e.g. thermal fluctuations, we could not use them for steering the intensities of the states according to Equation (27). In this case, the photodiodes have to be operated with as large as possible quantum efficiencies, and the three-state superposition has to be generated by splitting the photon into three beams, as in Figure 1.

4.2 Minimising setup's interaction with the environment

To observe deviations from Born's rule, we have to ensure that the displacement between States 0 and 1 is at the reduction point in time sufficiently large to fulfil the decorrelation criterion $\Delta s_1(\bar{t}_C) > 6\sigma_n$. Since the reduction point in time cannot be measured so far, we must forecast it as precisely as possible to ensure a sufficient displacement at this point in time. This is effected on the one hand by a precise calculation, taking all components of the setup into account (Section 5); and on the other hand, by minimising the setup's interaction with the environment during superposition. The second measure ensures that the environment, such as e.g. an observer, does not participate in quantum superposition and influence the reduction point in time. The minimisation of environmental interaction is addressed in our experiment by the following two measures.

1. Measurement after reduction instead of reduction by measurement

Since an observer, who tries to measure the result of the experiment directly, participates in quantum superposition and thus influences the reduction point in time, we take the result of our experiment a sufficient period of time after the three-state superposition of the solid has reduced. This is carried out by connecting after this period of time

voltmeters to the two capacitors in Figure 3, which are biasing Photodiode 1 and 2, and by checking whether their voltages have dropped due to an avalanche current in the corresponding photodiode. A voltage drop in Capacitor 2 corresponds to a reduction to State 2; a drop in Capacitor 1 to a reduction to State 1; and no drop to a reduction to State 0.

2. Plate capacitors as voltage supplies

Since the usual voltage supplies can interact with the environment up to the power plant, our avalanche photodiodes are not biased by such voltage supplies. Instead we use, as shown in Figure 3, simple plate capacitors, which are charged before the measurement by the usual voltage supplies, and which are disconnected from the voltage supplies shortly before the photon's arrival.

4.3 Measurement

In this section, we present the process of measurement.

Gated mode

Avalanche photodiodes can have breakthroughs even in the absence of photons. The probability of such *dark counts* increases with the photodiode's excess bias voltage V_E , i.e. how much the photodiode is biased above its breakdown voltage V_B . To avoid dark counts, the photodiodes can be operated in the so-called *gated mode* [17]. In the gated mode, the photodiodes are biased at the operating level $V_B + V_E$ only for a short period of time around the photon's arrival. Before the photon's arrival, we bias the photodiodes slightly below their breakdown voltages V_B . After the photon's arrival, we disconnect the photodiodes from their biasing plate capacitors, as will be explained subsequently.

Process

The process of a measurement is illustrated in Figure 4. The upper part of the figure shows the setup for charging the plate capacitors and for measuring the voltages at the plate capacitors after the photon's arrival. The lower part shows the voltage curve at the photodiode during a measurement and points in time t_i corresponding to steps of the measurement that will be explained later. At the beginning, the voltage supply is connected to the capacitor by closing the switches at 1, and the voltage at the capacitor is kept slightly below the photodiode's breakdown voltage V_B . At t_1 , shortly before the photon's arrival, the voltage is increased to $V_B + V_E$, and the voltage supply is then disconnected from the capacitor by opening the switches at 1. At t_2 , the photon enters the photodiode, and a short time afterwards the avalanche current starts at $t=0$. At t_3 , after the avalanche current has stopped, the photodiode is disconnected to suppress dark

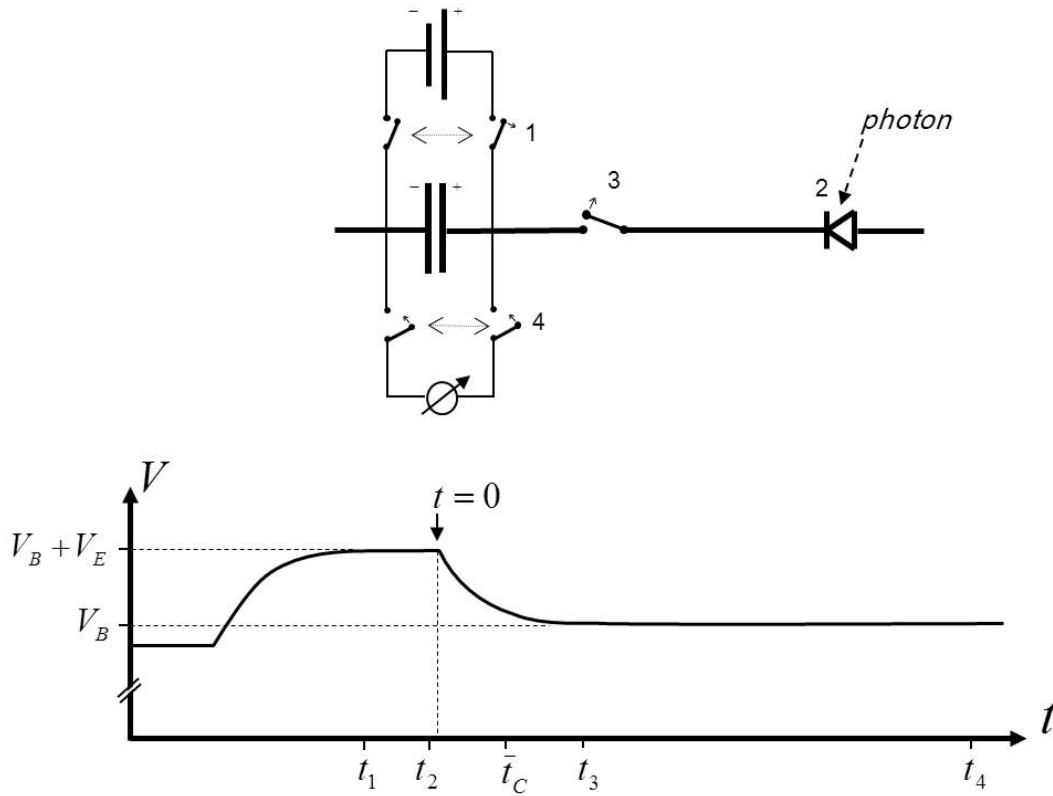


Fig. 4: *Upper:* Setup for charging the plate capacitors and for measuring the voltages at the plate capacitors after the photon's arrival.
Lower: Voltage curve at the photodiode and points in time t_i corresponding to steps of the measurement.

counts from the plate capacitor by opening the switch at 3. At t_4 , the voltmeter is connected to the capacitor by closing the switches at 4, and the result of the measurement is taken by checking whether the capacitor's voltage has dropped due to an avalanche current. The voltage drop is roughly $\Delta V \approx V_E \cdot C_p / (C + C_p)$, where C and C_p are the capacitances of the plate and the piezo capacitor, respectively. The four switches for disconnecting the voltage supply and the voltmeter from the setup during superposition in Figure 4 can be realised by field effect transistors of enhancement mode. For the execution of the measurement process, it is recommended to use computer-controlled voltage supplies and meters.

Reference measurement behaving in accordance with Born's rule

To check the increase of State 2's reduction probability with respect to Born's rule, we make a reference measurement, in which the reduction probability of State 2 behaves in accordance with Born's rule. This is effected by inserting an aperture before Photodiode 1, as shown in Figure 3. The photon is then measured by Photodiode 2 only, and the piezo capacitor evolves into a two-state superposition for which the reduction probability of State 2 behaves in accordance with Born's rule ($p_2 = I_2$).

4.4 Photodiodes

The proposed experiment can be realised with commercially available so-called *thick silicon SPADs* (single-photon avalanche photodiodes). In this section, we summarise the typical parameters of these photodiodes [18] that are used for the quantitative analysis in Section 5.

Photon's wavelength: Thick silicon SPADs are suitable for photon wavelength of $\lambda \approx 800nm$, for which they have quite good quantum efficiencies.

Breakdown voltage: The breakdown voltages of thick silicon SPADs are in the range between $250V-450V$. In our calculations, we assume $V_B = 420V$.

Excess bias voltage: Thick silicon SPADs can be operated with excess bias voltages V_E in the range of $1V-50V$.

Quantum efficiency: The SPADs' quantum efficiencies p_{QE} increase with the applied excess bias voltage V_E . In our calculations, we assume a quantum efficiency of $p_{QE} = 70\%$ for $V_E = 20V$, and a quantum efficiency of $p_{QE} = 35\%$ for $V_E = 10V$.

Dark count rate: The photodiode's dark count rate f_{DC} defining the rate of dark counts in the absence of photons increases also with the excess bias voltages V_E , and is smaller than $20kHz$ for $V_E = 20V$.

Time resolution: The time resolution Δt_{res} achieved in photon timing decreases over the excess bias voltages, and is typically $170ps$ for $V_E = 20V$.

Latching current level: The so-called latching current level, below which the avalanche current breaks down, is typically $I_q \approx 0.1mA$.

Resistance: The internal resistance of a thick silicon SPAD is typically lower than 500Ω . In our calculations, we assume $R_d = 500\Omega$.

5 Quantitative analysis

In this section, we calculate how the setup's components must be dimensioned and the operating parameters to be chosen to observe deviations from Born's rule. These calculations will demonstrate the feasibility of the experiment. In Section 5.1, we discuss the setup in Figure 3, in which the three-state superposition is generated with the help of the piezo capacitor. In Section 5.2, we discuss an alternative, in which a capacitor with movable plates is used for this purpose. In Section 5.3, we investigate how much the other components of the setup, such as the photodiodes, plate capacitors etc., influence the reduction point in time, and show that their impact is negligible if they are chosen suitably.

5.1 Setup with piezo capacitor

The quantitative analysis of the setup with the piezo capacitor in Figure 3 is performed in three steps. In Section 5.1.1, we derive formulae to calculate the setup's reduction point in time. In Section 5.1.2, we show how the setup must be dimensioned and the operating parameters must be chosen. In Section 5.1.3 we present the results of our calculations, which will demonstrate the feasibility of the proposed experiment.

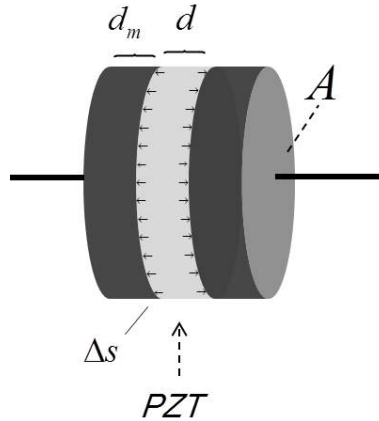


Fig. 5: Piezo capacitor.

5.1.1 Calculation of reduction point in time

Figure 5 shows details of the piezo capacitor. It has an area of A , its piezo a thickness of d , and its plates thicknesses of d_m .

Piezoes of PZT

To obtain sufficient displacements of the piezo capacitor's plates for fulfilling the decorrelation criterion $\Delta s_1(\bar{t}_C) > 6\sigma_n$, we require piezos with particularly large piezo electric

coefficients, given for piezoelectric ceramics of lead zirconium titanate (PZT). The calculations here refer to the product PIC-153 of PI Ceramic GmbH, which is used for piezoactuators [19]. For PIC-153, only the d_{33} -component of the matrix for the converse piezoelectric effect is relevant¹², which describes how much the piezo's thickness in the z-direction d changes when an electric field E in the same direction is applied, i.e. $\Delta d/d = d_{33}E$ [19]. PIC-153 has an extremely high d_{33} -coefficient (also denoted as the piezoelectric charge coefficient) of $d_{33} = 600 \cdot 10^{-10} V^{-1} cm$, accompanied by a very high relative permittivity of $\epsilon_r = 4200$ [19]¹³. When a voltage of V_i is applied to the piezo capacitor, its plates are displaced by

$$\Delta s_i = \frac{d_{33}}{2} V_i \quad , \quad (28)$$

which follows with $V = Ed$ and $\Delta s = \Delta d/2$, where E is the electric field inside the piezo. Equation (28) describes the displacement of a piezoactuator with one layer [20].

Displacement profiles $\Delta s_i(t)$

When the capacitances C of the plate capacitors biasing the photodiodes are much larger than that of the piezo capacitor C_p ($C \gg C_p$), the voltage profiles at the piezo capacitor in States 1 and 2, $V_1(t)$ and $V_2(t)$ are given by [18]:

$$V_i(t) = V_{Ei} \left(1 - e^{-\frac{t}{\tau_i}}\right) \quad \text{with} \quad \tau_1 = (R + R_d)C_p, \quad \tau_2 = R_d C_p \quad , \quad (29)$$

where V_{E1} and V_{E2} are the excess bias voltages applied to the photodiodes (see Figure 3), R_d the internal resistance of the photodiode, and R the resistance of the resistor behind Photodiode 1 in Figure 3. The capacitance of the piezo capacitor is given by $C_p = \epsilon_0 \epsilon_r A/d$. The displacement profiles $\Delta s_1(t)$ and $\Delta s_2(t)$ of the piezo capacitor's plates in State 1 and 2 follow by inserting Equation (29) into Equation (28). When the piezo capacitor is completely charged in State 2, its plates are displaced by

$$\Delta s_{2max} = \frac{d_{33} V_{E2}}{2} \quad . \quad (30)$$

Diósi-Penrose energies and competition actions of the piezo capacitor

The Diósi-Penrose energies of the piezo capacitor between the states E_{Gij}^s can be calculated with Equation (12), where the contribution of the capacitor's plates is calculated with a geometric factor of $\alpha_{geo} = 1$ (displaced plate), and the contribution of the piezo with $\alpha_{geo} = \frac{1}{3}$ (extended plate). In [3], it is shown that the Diósi-Penrose energy of

¹²The d_{31} - and the d_{15} -components of PIC-153 are not specified [19].

¹³An alternative to PIC-153 is PIC-152 with $d_{33} = 300 \cdot 10^{-10} V^{-1} cm$ and $\epsilon_r = 1350$, for which also only the d_{33} -component is relevant [19].

the piezo capacitor is given by the sum of the Diósi-Penrose energies of the piezo and of the two plates, when the size of the plates is much larger than the thicknesses of the piezo and the plates ($\sqrt{A} \gg d, d_m$). For displacements much larger than the mean lattice constant of the solid ($\Delta s_i \gg \bar{g}$), for which the short-distance contribution to the Diósi-Penrose energy $E_G^{Ss}(\Delta s)$ in Equation (12) can be neglected, the piezo capacitor's total Diósi-Penrose energies is given by

$$E_{Gij}^S(t) = 2\pi GA \left(\frac{1}{3} d \rho_p^2 + 2d_m \rho_m^2 \right) (\Delta s_i(t) - \Delta s_j(t))^2, \quad (31)$$

where ρ_p and ρ_m are the mass densities of the piezo and the plates. The displacement profile in State 0 is $\Delta s_0(t)=0$. The competition actions of the piezo capacitor $S_{Gij}^S(\bar{t})$ (from Equation 6) are

$$S_{Gij}^S(\bar{t}) = \int_0^{\bar{t}} dt E_{Gij}^S(t), \quad (32)$$

where $t=0$ corresponds to the point in time when the avalanche is triggered (cf. Figure 4).

Estimation of \bar{t}_C

The reduction point in time \bar{t}_C of the piezo capacitor in the three-state superposition can be estimated according to the calculations in Section 3.4 for the case " $\Delta s_2 \gg \Delta s_1$ " and also the more realistic case " $\Delta s_2/\Delta s_1=4$ " by $S_{G02}^S(\bar{t}_C) \approx \hbar$, i.e. when the competition action between Classical Scenarios 0 and 2 approximately reaches Planck's quantum of action. For the calculation of \bar{t}_C , we have to distinguish the cases where the charging of the piezo capacitor has finished before \bar{t}_C , or will finish after \bar{t}_C . When the charging has finished much before \bar{t}_C , the displacement profile in State 2 can be approximated by $\Delta s_2(t) \approx \Delta s_{2max}$. When it finishes long after \bar{t}_C , we can assume that $\Delta s_2(t) \approx \Delta s_{2max} \cdot t/\tau_2$ (cf. Equations 29 and 30). The area A of our piezo capacitor, for which the capacitor's charging finishes approximately at the reduction point in time, i.e. $\bar{t}_C \approx 2\tau_2$, is:

$$A_{max} = \sqrt{\frac{9\hbar}{\pi G \epsilon_0 \epsilon_r (1 + 6 \frac{d_m \rho_m^2}{d \rho_p^2}) R_d}} \frac{1}{\rho_p d_{33} V_{E2}}, \quad (33)$$

which follows with the approximation $\Delta s_2(t) \approx \Delta s_{2max} \cdot t/\bar{t}_C$ for the displacement profile. For the case $A < A_{max}/4$ (i.e. when the charging has finished before \bar{t}_C), $A \approx A_{max}$ (when the charging finishes at roughly \bar{t}_C), and $A > 2A_{max}$ (when the charging finishes after \bar{t}_C), the reduction points in time are given by:

$$\bar{t}_C \approx \begin{cases} \frac{6\hbar}{\pi G d \rho_p^2 (1 + 6 \frac{d_m \rho_m^2}{d \rho_p^2}) d_{33}^2 V_{E2}^2 A} & A < \frac{A_{max}}{4} \\ \sqrt{\frac{9\hbar \epsilon_0 R_d \epsilon_r}{\pi G (1 + 6 \frac{d_m \rho_m^2}{d \rho_p^2})}} \frac{1}{d \rho_p d_{33} V_{E2}} & A \approx A_{max} \\ \sqrt[3]{\frac{18\pi \epsilon_0^2 \epsilon_r^2 R_d^2 A}{\pi G \rho_p^2 (1 + 6 \frac{d_m \rho_m^2}{d \rho_p^2}) d_{33}^2 V_{E2}^2}} \frac{1}{d} & A > 2A_{max} \end{cases} . \quad (34)$$

The corresponding displacements Δs_2 of the piezo capacitor's plates in State 2 at these points in time are

$$\Delta s_2(\bar{t}_C) \approx \begin{cases} \frac{d_{33} V_{E2}}{2} & A \leq A_{max} \\ \sqrt[3]{\frac{9\pi V_{E2} d_{33}}{4\pi G \epsilon_0 \epsilon_r \rho_p^2 (1 + 6 \frac{d_m \rho_m^2}{d \rho_p^2}) R_d A^2}} & A > 2A_{max} \end{cases} . \quad (35)$$

The largest possible displacement of the capacitor's plates is $\Delta s_{2max} = d_{33} V_{E2} / 2$ (Equation 30), which we obtain for $A \leq A_{max}$. This means that the area A_{max} according to Equation (33) is the largest possible area of our piezo capacitor with which we can achieve the maximum displacement Δs_{2max} . This maximum displacement Δs_{2max} and the area A_{max} both depend on parameters of the photodiode, i.e. the excess bias voltage V_{E2} and the photodiode's internal resistance R_d (see Equations 30 and 33). One can excise this dependency by charging the piezo capacitor not with the photodiode's avalanche current, but, as shown in Figure 9, by a separate plate capacitor, which is connected to the piezo capacitor with the help of a field effect transistor whose gate is steered by the photodiode's avalanche current. The excess bias voltage V_{E2} and the internal resistance R_d in Equations (30) and (33)-(35) then have to be replaced by the voltage V_2 of the separate plate capacitor and the internal resistance of the field effect transistor connecting the plate capacitor with the piezo capacitor (see Figure 9).

5.1.2 Choice of parameters

In this section, we show how the setup must be dimensioned and the operating parameters must be chosen to observe deviations from Born's rule. For the experimenter, it is important to note that the calculation of the operating parameters and of the dimensioning of the piezo capacitor can be performed with the approximation formulae derived here, and do not require numerical calculations. These are Equations (21) and (27) for the calculation of the expected increase of State 2's reduction probability with

respect to Born's rule p_2/I_2 , and Equations (33)-(35) for the calculation of the reduction point in time \bar{t}_C and the displacement $\Delta s_2(\bar{t}_C)$ in State 2 at this point in time.

Excess bias voltages: We size our experiment such that we obtain a displacement ratio of about $\Delta s_2/\Delta s_1 \approx 4$ at the reduction point in time, which is (according to our calculations in Section 3.4) sufficient to obtain a significant increase of State 2's reduction probability with respect to Born's rule. For higher displacement ratios, it is more difficult to satisfy the decorrelation criterion $\Delta s_1(\bar{t}_C) > 6\sigma_n$. To obtain in State 2 a larger displacement than in State 1 ($\Delta s_2 > \Delta s_1$), we choose the excess bias voltage of Photodiode 2 with $V_{E2} = 20V$ to be larger than that of Photodiode 1 with $V_{E1} = 10V$, which leads, with $\Delta s_i \approx d_{33} V_{Ei} / 2$ (cf. Equations 28 and 30), to a displacement ratio of about $\Delta s_2/\Delta s_1 \approx 2^{14}$. To obtain the displacement ratio of $\Delta s_2/\Delta s_1 \approx 4$, we additionally insert the resistor R behind Photodiode 1 (see Figure 3), whose resistance will be calculated below.

Beam splitter: From Equation (21), it follows that the absolute increase of State 2's reduction probability with respect to Born's rule $p_2 - I_2$ is highest for an intensity I_2 of State 2 on the interval $[0.25, 0.6]$. The intensity of State 2 depends on the reflection coefficient R^2 of the beam splitter and the quantum efficiency p_{QE2} of Photodiode 2 as $I_2 = R^2 p_{QE2}$, where the quantum efficiency p_{QE2} is determined by the photodiode's excess bias voltage V_{E2} (cf. Section 4.4). The reflection coefficient R^2 of the beam splitter should therefore be chosen in such a way that I_2 is on the interval $[0.25, 0.6]$. The intensities I_0 and I_1 of States 0 and 1 have, according to Equation (21), no influence on the increase of State 2's reduction probability and do not require special attention. The reason for this is explained in [1, 2].

For our calculations, we choose $R^2 = 30\%$ and $T^2 = 70\%$, which leads with the quantum efficiencies $p_{QE2} = 70\%$ and $p_{QE1} = 35\%$ following from the photodiodes' excess bias voltages of $V_{E2} = 20V$ and $V_{E1} = 10V$ (cf. Section 4.4) to an intensity vector of $\vec{I} = (0.545, 0.245, 0.21)^T$ (cf. Equation 27), which is close to the intensity vector $\vec{I} = (\frac{1}{2}, \frac{1}{4}, \frac{1}{4})^T$ that was used for the calculation of the case " $\Delta s_2/\Delta s_1 = 4$ " in Section 3.4. The intensity of State 2 is with $I_2 = 0.21$ close to the interval $[0.25, 0.6]$.

Plates of the piezo capacitor: According to Equation (33), the area A_{max} to achieve the maximum displacement $\Delta s_{2,max}$ decreases with the mass density ρ_m of the piezo capacitor's plates. Therefore, it is recommended to use plates with a small mass density. For our calculations, we assume plates of aluminium.

Dimensions of the piezo capacitor: The area of our piezo capacitor A is chosen to be close to the area A_{max} for achieving the maximum displacement $\Delta s_{2,max}$ according to Equation (33). For the calculation of A_{max} , we assume that the thickness of the piezo d is twice as large as those of the plates d_m ($d = 2d_m$). From Equation (33) for A_{max} , we get with the mass densities of PZT and aluminium of $\rho_{PZT} = 7.6g/cm^3$ and $\rho_{Al} = 2.7g/cm^3$, the parameters of PIC-153 (cf. Section 5.1.1), the excess bias voltage of Photodiode 2 of $V_{E2} = 20V$, and an internal resistance of the photodiode of $R_d = 500\Omega$, an

¹⁴ Note that a lower excess bias voltage of Photodiode 1 of e.g. only $V_{E1} = 5V$ leads to a lower quantum efficiency of this photodiode.

area A_{max} , which corresponds to a disc with a diameter of $2.4mm$. For our calculations, we assume a PZT disc with a diameter of $3mm$ and a thickness of $d=0.2mm$, which is the smallest standard dimension offered by PI Ceramic GmbH [19]. The thicknesses of the aluminium plates are $d_m=d/2=0.1mm$. For these parameters, our piezo capacitor has a capacitance of $C_p=1300pF$.

Resistor behind Photodiode 1: The resistance of the resistor R behind Photodiode 1 in Figure 3 is chosen such that we obtain the displacement ratio of $\Delta s_2/\Delta s_1=4$ at the reduction point in time. This leads to the condition $V_2(\bar{t}_C)/V_1(\bar{t}_C)=4^{15}$ (cf. Equations 28 and 29). The reduction point in time \bar{t}_C follows with Equation (34) for $A\approx A_{max}$ to be $\bar{t}_C\approx 0.86\mu s$. This leads with $V_{E2}=20V$, $V_{E1}=10V$, $R_d=500\Omega$ and $C_p=1300pF$ to a resistance of $R=940\Omega$.

5.1.3 Feasibility

In this section, we present the results following from the choice of parameters of Section 5.1.2, which will demonstrate the feasibility of the experiment. We will calculate the results on the one hand with our approximation formulas and compare them to the exact numerical calculations, which take all discussed details into account. The comparison of the results will show that our approximation formulae are sufficient for the dimensioning of the experiment. Figure 6 displays the chosen parameters and the calculated results.

Rough calculation: With the approximation formula for \bar{t}_C (Equation 34), we obtain for $A\approx A_{max}$ a reduction point in time of $\bar{t}_C=0.86\mu s$, and with the approximation formula for p_2 (Equation 21) with $I_2=0.21$ an increase of State 2's reduction probability with respect to Born's rule of $p_2/I_2=1.65$. The displacement in State 2 at the reduction point in time follows with Equation (35) for $A\leq A_{max}$ to be $\Delta s_2(\bar{t}_C)=60\text{\AA}$. The displacement in State 1 is, according to our choice of R in Section 5.1.2, four times smaller; i.e. $\Delta s_1(\bar{t}_C)=15\text{\AA}$.

Exact numerical calculation: When we calculate \bar{t}_C and p_2 with the procedure described at the beginning of Section 3.4 and calculate the piezo capacitor's Diósi-Penrose energies with Equation (31), in which the short-distance contributions to the Diósi-Penrose energies are neglected (cf. Section 3.3), we obtain $\bar{t}_C=0.87\mu s$ and $p_2/I_2=1.49$. When we take the short-distance contributions to the Diósi-Penrose energies of the piezo and the plates according to Equation (13) additionally into account¹⁶, we obtain $\bar{t}_C=0.84\mu s$, $p_2/I_2=1.56$ and displacements of $\Delta s_2(\bar{t}_C)=43.3\text{\AA}$ and $\Delta s_1(\bar{t}_C)=10.7\text{\AA}$, as shown in Figure 6. The short-distance contributions to the Diósi-Penrose energy do not change the result very much, since the displacements Δs_2 and Δs_1 are significantly

¹⁵I.e. $V_{E2}(1 - e^{-\frac{\bar{t}_C}{R_d C_p}}) = 4V_{E1}(1 - e^{-\frac{\bar{t}_C}{(R_d + R)C_p}})$.

¹⁶The short-distance contribution to the Disi-Penrose energy of the plates is calculated with the geometric function $F_{geo}(x)$ for the displaced plate and $\bar{T}_G^S/\hbar=4.3MHz/cm^3$, $\sigma_n=0.1\text{\AA}$ for aluminium [3]. The short-distance contribution of the piezo is calculated with the geometric function for the extended plate and $\bar{T}_G^S/\hbar=71.8MHz/cm^3$, $\sigma_n=0.095\text{\AA}$ for PZT [3].

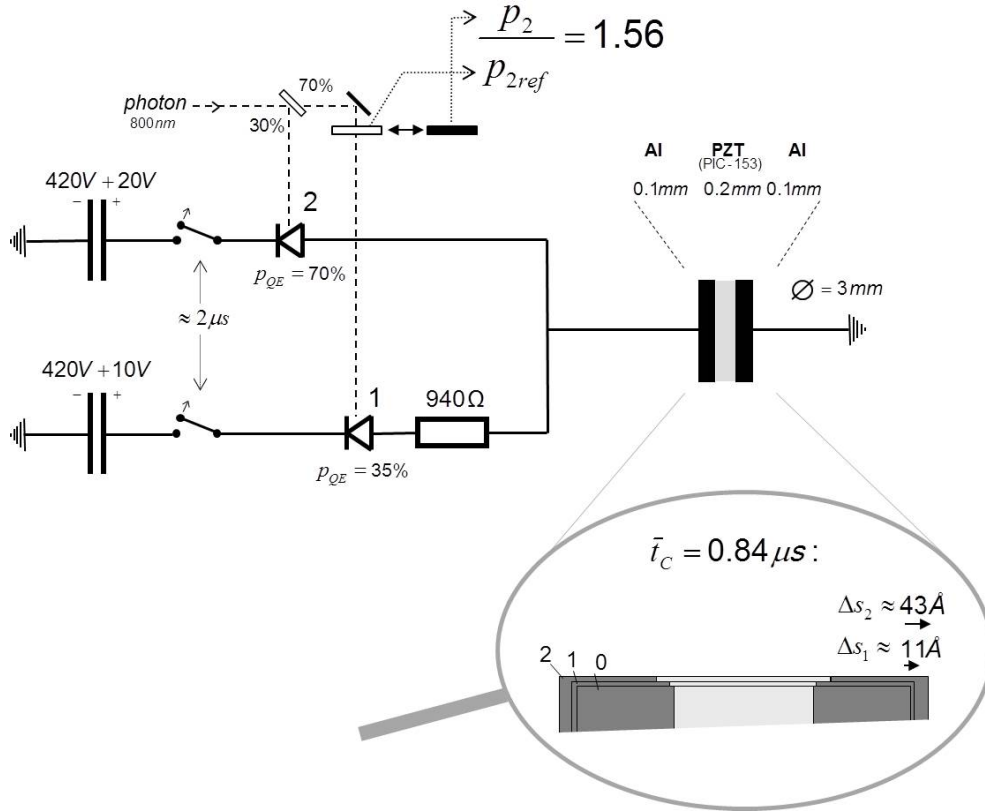


Fig. 6: Chosen parameters and calculated result of the experiment in Figure 3. The detection probability in Photodiode 2 increases by a factor of 1.56 when the aperture before Photodiode 1 is removed. The inset shows the displacements of the plates in States 1 and 2 at the reduction point in time \bar{t}_C .

larger than the mean lattice constants ($\Delta s_i \gg \bar{g}$; cf. Section 3.3), which are $\bar{g} = 2.42 \text{ \AA}$ and $\bar{g} = 2.55 \text{ \AA}$ for PZT and aluminium, respectively [3].

Fulfilment of the decorrelation criterion: The displacement between States 0 and 1 at the reduction point in time is $\Delta s_1(\bar{t}_C) = 10.7 \text{ \AA}$; sufficiently large to fulfil the decorrelation criterion $\Delta s_1(\bar{t}_C) > 6\sigma_n$. The spatial variation of the nuclei of aluminium and PZT is respectively $\sigma_n \approx 0.1 \text{ \AA}$ and $\sigma_n \approx 0.095 \text{ \AA}$ at room temperature [3].

Breakdown of the avalanche currents: For the chosen parameters, the three-state superposition of the piezo capacitor reduces before the breakdowns of the avalanche currents in Photodiodes 2 and 1, which happen at $t_q \approx 4 \mu s$ and $t_q \approx 8 \mu s$ when the avalanche currents in Photodiodes 2 and 1 fall below the latching current level of $I_q \approx 0.1 \text{ mA}$.

Settling time of the piezo capacitor: The settling time for the displacement of the piezo capacitor's plate is smaller than the expected reduction point in time of $\bar{t}_C \approx 1 \mu s$. The typical working frequencies of piezoactuators of PZT reach up to 3 MHz [19]. This means that the time delays occurring between voltage changes at the piezo capacitor and the displacements of its plates can be neglected. The settling time resulting from

the finite sound velocities in PZT and in the aluminium plates is $\Delta t \approx 0.05 \mu s$ ¹⁷.

Time resolution of the photodiodes: The photodiodes' time resolutions are, at typically $170 ps$, significantly smaller than the expected reduction point in time, and play no further role in our discussion.

Dark counts: From the time constant for charging the piezo capacitor in State 2 of $\tau_2 = R_d C_p = 0.65 \mu s$ and the reduction point in time of $\bar{t}_C \approx 1 \mu s$, it follows that the photodiodes can be disconnected from their biasing plate capacitors after roughly $2 \mu s$, as shown in Figure 6. This leads with $f_{DC}(x) < 20 kHz$ for $V_E = 20V$ (cf. Section 4.4) to a dark count probability p_{DC} smaller than 0.04 ($p_{DC} = f_{DC} \cdot 2 \mu s$).

Number of measurements needed: For the reference measurement at which we insert the aperture before Photodiode 1 in Figure 6, the detection probability in Photodiode 2 behaves in accordance with Born's rule and is $p_{2ref} = I_2 = 0.21$. When we remove the aperture, the detection probability in Photodiode 2 increases from 0.21 to $p_2 = I_2 \cdot 1.56 = 0.33$. From these numbers and a dark count probability p_{DC} smaller than 0.04, it follows that the predicted increase of Photodiode 2's detection probability of $p_2 / p_{2ref} = 1.56$ can be checked by a few hundred statistically significant measurements.

¹⁷This follows with $\Delta t \approx d / (2v_{||}^{PZT}) + d_m / v_{||}^{Al}$ [3] and sound velocities of $v_{||}^{PZT} = 2910 m/s$ and $v_{||}^{Al} = 6420 m/s$ for PZT and aluminium, respectively [3].

5.2 Setup with a capacitor with movable plates

In this section, we discuss an alternative to the setup in Figure 3, in which we use a capacitor with movable plates (instead of the piezo capacitor) to allow a solid to evolve into a three-state superposition. Such a capacitor is shown in Figure 7, whose plates move towards each other by the electric force between the plates when the capacitor is charged. The capacitor's plates have an area of A , a distance of d and thicknesses of d_m , as shown in Figure 7.

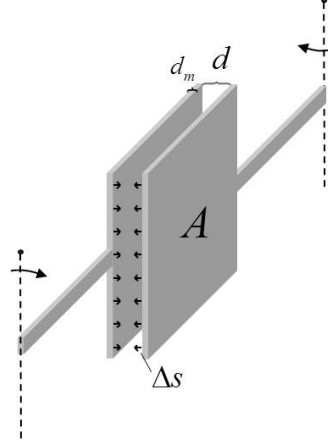


Fig. 7: Capacitor with movable plates.

Reduction point in time

For our choice of parameters, the time constant for charging the capacitor with movable plates will be significantly smaller than the reduction point in time, which allows us to simplify the voltage profiles at the capacitor by $V_i(t) = V_{Ei}$. This leads to the following displacement profiles in States 1 and 2 ($i=1, 2$)¹⁸:

$$\Delta s_i(t) = \frac{\epsilon_0 V_{Ei}^2}{2d^2 d_m \rho_m} t^2 . \quad (36)$$

With a calculation similar to that in Section 5.1.1 using Equation (31) with $\rho_p = 0$ to estimate the Diósi-Penrose energies E_{Gij}^S of the capacitor with movable plates, and with the condition $S_{G02}^S(\bar{t}_C) \approx \hbar$ to determine the reduction point in time, we obtain the following reduction point in time:

$$\bar{t}_C = \sqrt[5]{\frac{5\hbar d^4 d_m}{\pi G \epsilon_0^2 A V_{E2}^4}} . \quad (37)$$

The displacement Δs_2 in State 2 at this point in time is given by

$$\Delta s_2(\bar{t}_C) = \sqrt[5]{\frac{25\epsilon_0 \hbar^2 V_{E2}^2}{32\pi^2 G^2 d^2 d_m^3 A^2}} \frac{1}{\rho_m} . \quad (38)$$

¹⁸This follows with $F = M\Delta\ddot{s}$, $M = Ad_m\rho_m$, $F = EQ$, $Ed = V_E$, $Q = V_E C$ and $C = \epsilon_0 A/d$.

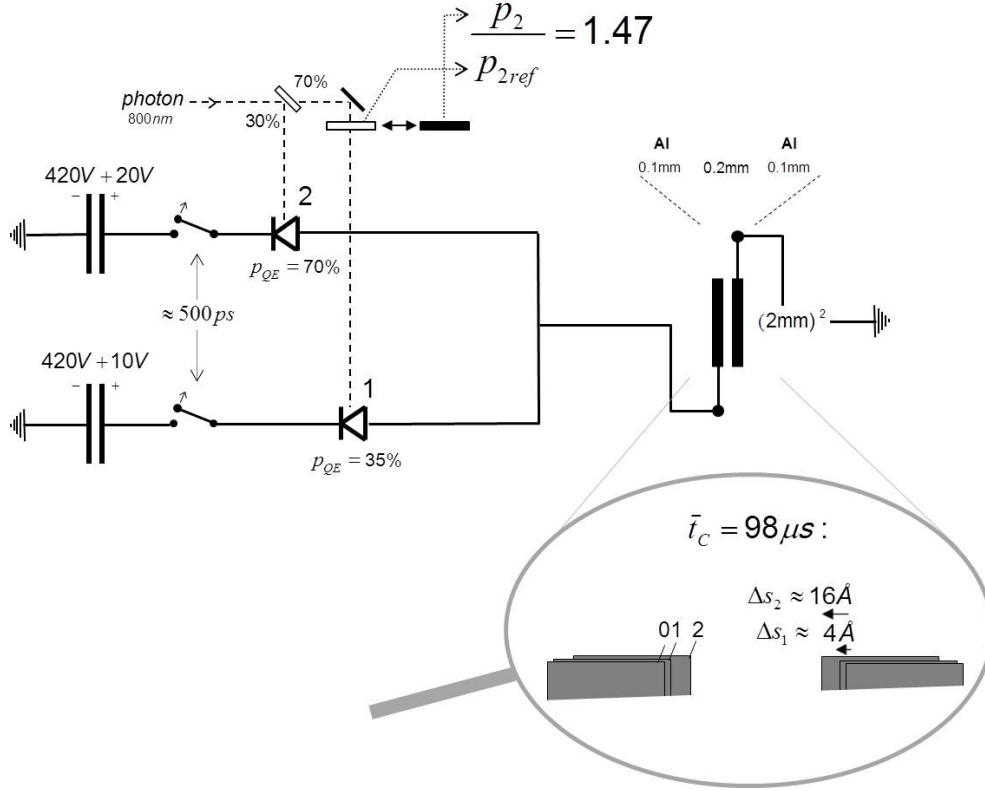


Fig. 8: Chosen parameters and calculated result for a setup using the capacitor with movable plates in Figure 7 to allow a solid evolve into a three-state superposition. The detection probability in Photodiode 2 increases by a factor of 1.47 when the aperture before Photodiode 1 is removed. The inset shows the displacements of the plates in States 1 and 2 at the reduction point in time \bar{t}_C .

Choice of parameters

From Equation (38), it follows that the displacement between States 0 and 2 at the reduction point in time $\Delta s_2(\bar{t}_C)$ decreases with the mass density ρ_m , the area A , the thicknesses d_m of the plates, and also with the distance d between the plates. This leads us to choose aluminium plates with a small mass density ρ_m , and to a small capacitor size: $A=(2\text{mm})^2$, $d_m=0.1\text{mm}$ and $d=0.2\text{mm}$, as displayed in Figure 8. The excess bias voltages of the photodiodes are chosen as $V_{E1}=10\text{V}$ and $V_{E2}=20\text{V}$, which leads, according to Equation (36), to a displacement ratio of $\Delta s_2/\Delta s_1=4$ at all times. A resistor behind Photodiode 1, as in the setup in Figure 3, is not needed.

Feasibility

For our choice of parameters, we obtain with Equations (37) and (38) a reduction point in time of $\bar{t}_C \approx 96\mu\text{s}$ and a displacement between States 0 and 2 at this point in time of $\Delta s_2(\bar{t}_C) \approx 15\text{\AA}$. The increase of State 2's reduction probability follows with Equation (21) and $I_2=0.21$ to be $p_2/I_2=1.65$. The exact procedure for calculating \bar{t}_C and p_2 according to Section 3.4, taking the short-distance contribution to the Diósi-Penrose energies of the plates into account, gives $\bar{t}_C=98\mu\text{s}$, $p_2/I_2=1.47$, $\Delta s_2(\bar{t}_C)=15.8\text{\AA}$ and $\Delta s_1(\bar{t}_C)=3.95\text{\AA}$,

as shown in Figure 8. The displacement between States 0 and 1 at the reduction point in time of $\Delta s_1(\bar{t}_C)=3.95\text{\AA}$ is still sufficiently large to fulfil the decorrelation criterion $\Delta s_1(\bar{t}_C)>6\sigma_n$ ($\sigma_n=0.1\text{\AA}$ for aluminium).

The time constant for charging the capacitor with movable plates is $\tau=89\text{ps}$ ¹⁹, significantly smaller than the reduction point in time of $\bar{t}_C\approx 100\mu\text{s}$, which justifies the approach $V_i(t)=V_{Ei}$ for the voltage profiles. The short charging time allows us to disconnect the photodiodes from their biasing plate capacitors after 500ps , as shown in Figure 8, which suppresses the dark count probability p_{DC} to a minimum.

The chosen parameters and calculated results for the experiment with the movable plates capacitor are displayed in Figure 8.

¹⁹ $\tau=R_d C$ with $R_d=500\Omega$ and $C=\epsilon_0 A/d$.

5.3 Impact of the other components

In this section, we investigate the influence of the other components of the setup on the reduction point in time, such as the photodiodes, the biasing plate capacitors, etc., and give recommendations on how to choose them. For the biasing plate capacitors, it is recommended not to use electrolytic capacitors, but instead simple plate capacitors with dielectrics of corundum; and for the resistor R behind Photodiode 1 not commercially available metal-film resistors, but instead a rod of doped silicon.

Characteristic lifetime T_G of a component

The other components of our setup that are used to let the piezo capacitor evolve into a three-state superposition, such as the photodiodes, the biasing plate capacitors, the resistor behind Photodiode 1, etc., belong in the thought experiment in Figure 1 to one of the two detectors, whose Diósi-Penrose energies are described by Equation (3), where the Diósi-Penrose energies E_{Gi} of a component i depend on the mass distributions in the detection $\rho_{det}(\mathbf{x})$ and no-detection states $\rho_{no-det}(\mathbf{x})$ of the component (cf. Equation 3). To simplify our discussion, we ignore the time-dependencies of these Diósi-Penrose energies, and calculate the Diósi-Penrose energy E_{Gi} for every component after the settling time of detection. With the Diósi-Penrose criterion $T_G = \hbar/E_G$, we can characterise every component by a characteristic lifetime T_{Gi} that corresponds to the lifetime of the two-state superposition of the detection and no-detection states after the settling of this component ($T_{Gi} = \hbar/E_{Gi}$).

The contribution of Detectors 1 and 2 to the total competition action at the reduction point in time in Equation (14) $S_G^{Di}(\bar{t}_C)$ can be calculated with the characteristic lifetimes of its components T_{Gi} by

$$S_G^D(\bar{t}_C) \approx \hbar \sum_i \frac{\bar{t}_C}{T_{Gi}} . \quad (39)$$

When the characteristic lifetimes of the components T_{Gi} are significantly larger than the reduction point in time \bar{t}_C ($T_{Gi} \gg \bar{t}_C$), their impacts on \bar{t}_C are negligible.

Calculation of the components' lifetimes in [3]

The calculation of the components' characteristic lifetimes T_{Gi} requires a detailed analysis of all physical processes that can change the mass distribution $\rho_{det}(\mathbf{x})$ in the detection state of the component. This analysis is carried out in [3], in which the lifetime of a single-photon detector is calculated, which consists of the same components as our setup. The calculations in [3] are therefore, apart from the chosen parameters, identical to ours. Hence, we restrict ourselves here to the results of these calculations, and refer the reader for further details to [3].

The calculations in [3] show that the displacements between the nuclei in the detection and no-detection states of the component are much smaller than the nuclei's spatial

variations of about $\sigma_n \approx 0.1\text{\AA}$. In this limiting case, the Diósi-Penrose energy of the component is dominated (according to the discussion in Section 3.3) by the short-distance contribution, which can be calculated with Equation (13) for $\Delta s \ll \sigma_n$.

Plate capacitors

The voltages at the biasing plate capacitors are slightly decreased when they have finished charging the piezo capacitor. Due to the electric forces between the capacitor's plates, its dielectric is compressed, and we have in the no-detection state with a voltage of $V_B + V_E$ a slightly larger compression than in the detection state with a voltage of $V_B + V_E - \Delta V$ ($\Delta V \approx V_E \cdot C_p / (C + C_p)$; cf. Section 4.3). The formula for the Diósi-Penrose energy of a plate capacitor in a two-state superposition with different voltages is derived in [3]. To obtain a large characteristic lifetime T_G of the plate capacitor, it is recommended to use dielectrics of corundum (Al_2O_3), which has a modulus of elasticity of about $E_e \approx 350 - 406 \text{ GPa}$ [21].

For the voltage profiles in Equation (29), it is assumed that the capacitances of the plate capacitors C are much larger than that of the piezo capacitor C_p ($C \gg C_p$). The piezo capacitor in Figure 6 has a capacitance of $C_p = 1300 \text{ pF}$. For a plate capacitor with an area of $(9 \text{ cm})^2$ and a thickness of 1 mm , we obtain with $\epsilon_r \approx 9$ for corundum [21] a capacitance of $C \approx 650 \text{ pF}$. To satisfy $C \gg C_p$, we have to connect approximately 18 of such capacitors in parallel. The voltage for these 18 plate capacitors in parallel for biasing Photodiode 2 will decrease from $420 \text{ V} + 20 \text{ V}$ to approximately $420 \text{ V} + 18 \text{ V}$ after the piezo capacitor is charged. With the formula for the Diósi-Penrose energy of a plate capacitor in a two-state superposition in [3], we obtain a characteristic lifetime of the 18 plate capacitors in parallel of $T_G \approx 100 \text{ ms}$, where plates of copper with thicknesses of 0.03 mm are assumed.

When the capacitances of the biasing plate capacitors are not significantly larger than that of the piezo capacitor ($C \gg C_p$), one has to make the substitutions $V_{Ei} \rightarrow \alpha V_{Ei}$ and $C_p \rightarrow \alpha C_p$ with $\alpha = C / (C + C_p)$ in Equation (29). This leads to the substitutions $V_{E2} \rightarrow \alpha V_{E2}$ and $\epsilon_r \rightarrow \alpha \epsilon_r$ in Equations (33)-(35) for estimating the reduction point in time and the displacement at this point in time.

Resistor, photodiodes, wires and switches

The photodiodes, the resistor, the wires (connecting the components) and the two switches in Figure 6 will have in the detection state a slightly larger thermal expansion due to the heat energy that is generated by the avalanche current in photon detection. The formulae for the Diósi-Penrose energies of these components in two-state superpositions with a slightly larger thermal expansion in the detection than in the no-detection state are derived in [3]. The heat energy that is generated by the avalanche current is given by $R \int_0^{t_q} dt I(t)^2$, where $I(t)$ is the avalanche current's profile, t_q the point in time at which the avalanche breaks down, and R the resistance of the component. In the calculations of the following results, we used $\int_0^{t_q} dt I(t)^2 \approx 500 (\text{mA})^2 \mu\text{s}$ following

from the avalanche current profile $I(t)$ in Photodiode 2 in the experiment in Figure 6, which breaks down at $t_q \approx 4\mu s$ (cf. Section 5.1.3).

Resistor: In [3], it is shown that the Diósi-Penrose energy of a resistor depends on the resistivity ρ_Ω of the used material as $E_G \propto \rho_\Omega^{-1}$. To obtain large characteristic lifetimes T_G , it is recommended not to use commercially available metal-film resistors with resistivities of about $\rho_\Omega \approx 10^{-6}\Omega cm$, but instead a rod of doped silicon, with a much higher resistivity of e.g. $\rho_\Omega \approx 5\Omega cm$ corresponding to n-type doped silicon with a doping concentration of roughly $10^{15}/cm^3$ [21]. The 940Ω -resistor in Figure 6 can then be realised by a rod of diameter of $2mm$ and a length of approximately $6cm$. With the formulae derived in [3], we obtain a characteristic lifetime of $T_G \approx 1s$ for this component.

Photodiodes: The adaption of the calculation of the characteristic lifetime of the photodiode of the single photon detector in [3] yields, for our avalanche current profile of $\int_0^{t_q} dt I(t)^2 \approx 500(mA)^2 \mu s$, a characteristic lifetime of about $T_G \approx 1s$.

Wires: For the wires connecting the components of our setup in Figure 6, we regard representative a wire of copper with a length of $200cm$, a diameter of $1mm$, and an effective length of $l_e = 4cm$, where the effective length l_e is defined in [3]. With the formulae in [3], we obtain a characteristic lifetime of about $T_G \approx 10^7 s$.

Switches: The characteristic lifetimes of the switches in Figure 6 for disconnecting the photodiodes from the biasing plate capacitors after photon detection, which can be realised by field effect transistors of depletion mode, are expected to be in between those of the 940Ω -resistor ($T_G \approx 1s$) and the wires ($T_G \approx 10^7 s$).

6 Pursuing experiments

In this section, we take a look on pursuing experiments that were proposed in [1, 2] to check further aspects of the Dynamical Spacetime approach. For these experiments, we propose concrete setups and show their feasibility. In Section 6.1, we discuss an experiment for measuring the lifetime of a two-state superposition. In Section 6.2, we discuss the signalling experiment proposed in [1, 2] for checking the quasi-abrupt reconfigurations of the wavefunction's evolution in the Dynamical Spacetime approach, which can cover far-separated regions.

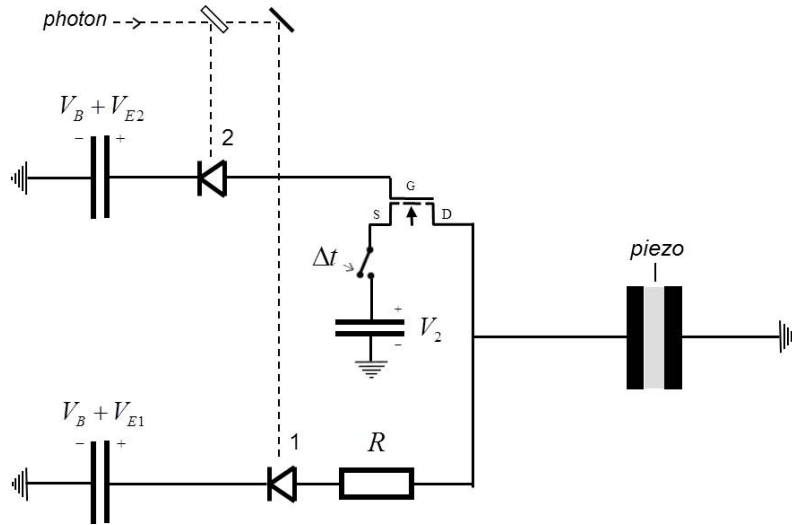


Fig. 9: Modification of the setup in Figure 3 to measure the lifetime of the two-state superposition of States 0 and 1.

6.1 Lifetime of a two-state superposition

In [1, 2], an experiment is proposed for measuring the lifetime of a two-state superposition with the help of the deviations from Born's rule predicted by the Dynamical Spacetime approach. If one allows the solid in Figure 1 first to evolve into a two-state superposition by delaying the displacement Δs_1 between States 0 and 1 by a time delay of Δt , one observes an increased reduction probability of State 2 only, when the two-state superposition of States 0 and 2 has not reduced before Δt . By measuring the reduction probability of State 2 over the time delay Δt , one can determine the lifetime of the two-state superposition. This procedure allows one not only to check whether the reduction point in time \bar{t}_C follows the Diósi-Penrose criterion $\bar{t}_C \approx \hbar/E_G$, but also to check the most important prediction of the Dynamical Spacetime approach: that collapse is not possible at any point in time (as in dynamical reduction models [7]), but only at specified points in time: the reduction points in time \bar{t}_C . The reduction probability of State 2 over Δt must therefore decrease abruptly at the reduction point in time \bar{t}_C of the two-state superposition.

Figure 9 shows how the setup in Figure 3 has to be modified for this experiment. Different to that described above, we measure the lifetime of the two-state superposition of States 0 and 1 and delay the displacement Δs_2 between States 0 and 2 by Δt . This is realised by allowing the avalanche current of Photodiode 2 open the gate of a field effect transistor of enhancement mode, which connects the piezo capacitor with the plate capacitor with the voltage V_2 in Figure 9, which is used for charging. The time delay is realised with the switch between the plate and the piezo capacitor, which is closed after the time delay Δt , as shown in Figure 9.

The lifetime, respectively the reduction point in time \bar{t}_C , of the two-state superposition of States 0 and 1 can be varied by the choice of the resistance R behind Photodiode 1, where one has to take care that the displacement between States 0 and 1 is (at the reduction point in time) still sufficiently large to fulfil the decorrelation criterion $\Delta s_1(\bar{t}_C) > 6\sigma_n$. The voltage V_2 of the plate capacitor for charging the piezo capacitor has to be chosen in such a way that the displacement $\Delta s_2 = d_{33} V_2 / 2$, which is achieved when the switch is closed (cf. Equation 30), is at least four times larger than that between States 0 and 1 ($\Delta s_2 > 4\Delta s_1(\bar{t}_C)$) to observe a significant increase of State 2's reduction probability for $\Delta t < \bar{t}_C$.

6.2 Signalling experiment

In [1, 2], it is shown that the deviations from Born's rule in the Dynamical Spacetime approach lead to superluminal signalling. This does not lead to a conflict with relativity, since causality evolves in the Dynamical Spacetime approach not along free selectable Lorentz frames in spacetime, but is parametrised by its expansion and evolves quasi-orthogonal to it [1, 2].

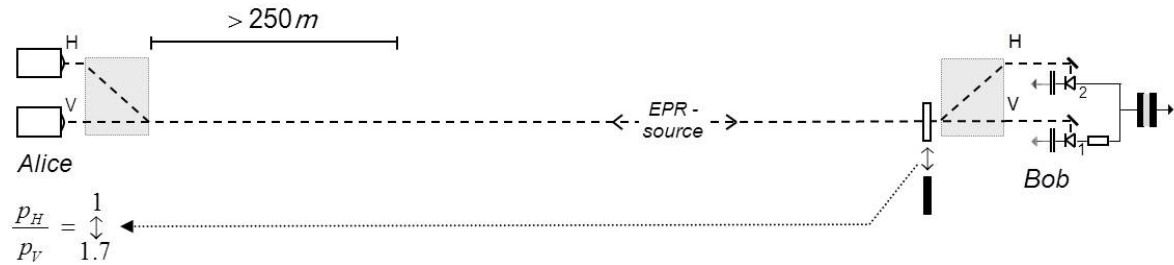


Fig. 10: Signalling experiment by inserting the setup of Figure 6 into an EPR experiment. Bob can manipulate the ratio between the polarisation probabilities measured by Alice from usually $p_H/p_V=1$ to $p_H/p_V \approx 1.7$ by removing the aperture.

A signalling experiment can be constructed by inserting the setup of Figure 6 into an EPR experiment, as shown in Figure 10. The setup puts Bob in a position to change the ratio between the polarisation probabilities measured by Alice from usually $p_H/p_V=1$ to $p_H/p_V \approx 1.7$, when he removes the aperture before his apparatus. This enables him to signal information to Alice. When the aperture is removed, the piezo capacitor on Bob's side evolves into a three-state superposition, which increases for a Bell state

of $|\psi\rangle=|H\rangle|H\rangle+|V\rangle|V\rangle$ the reduction probability of the $|H\rangle|H\rangle$ -part. Since the quasi-abrupt reconfiguration of the wavefunction's evolution also covers Alice's side, the polarisation of Alice's photon changes instantaneously, according to the reduction in the piezo capacitor. This happens before the photon arrives at Alice's detectors, when her arm is chosen to be at least

$$\delta > c\bar{t}_c \quad (40)$$

longer than Bob's arm. For the reduction point in time of our setup of $\bar{t}_c=0.84\mu s$, we obtain $\delta>250m$, as shown in Figure 10. Photons with a wavelength of approximately $\lambda\approx 800nm$ for our setup in Figure 6 can be generated by the usual parametric down-conversion of photons with wavelengths of $\lambda=404nm$. The ratio p_H/p_V between the polarisation probabilities (when the aperture is removed) can be calculated with Equation (21) as:²⁰

$$\frac{p_H}{p_V} \approx 1 + p_{QE2} \quad (41)$$

This leads, for the quantum efficiency of Photodiode 2 in Figure 6 of $p_{QE2}=70\%$, to $p_H/p_V\approx 1.7$, as shown in Figure 10.

²⁰From Equation (21) for the case " $\Delta s_2 \gg \Delta s_1$ " in Section 3.4, it follows that the reduction probabilities of States 0, 1 and 2 are given by:

$$p_0 = \frac{I_0}{1+I_2}, p_1 = \frac{I_1}{1+I_2}, p_2 = \frac{2I_2}{1+I_2}.$$

With this result, the probabilities p_{H2} , p_{H0} , p_{V1} and p_{V0} change as:

$$p'_{H2} = \frac{2p_{H2}}{1+p_{H2}}, p'_{H0} = \frac{p_{H0}}{1+p_{H2}}, p'_{V1} = \frac{p_{V1}}{1+p_{H2}}, p'_{V0} = \frac{p_{V0}}{1+p_{H2}},$$

where p_{H2} refers to the case that Alice measures an H-polarisation and Bob a photon detection by photodiode 2, and p_{H0} to the case that Bob measures no photon etc. With $p_H=p_{H2}+p_{H0}$, $p_V=p_{V1}+p_{V0}$, $p'_H=p'_{H2}+p'_{H0}$, $p'_V=p'_{V1}+p'_{V0}$ and $p_H=p_V=\frac{1}{2}$, we obtain $p'_H/p'_V=1+2p_{H2}$, which leads with $p_{H2}=\frac{1}{2}p_{QE2}$ to Equation (41).

7 Discussion

Our study has shown that the deviations from Born's rule predicted by the Dynamical Spacetime approach can be verified by quite simple experiments, which mostly use commercially available single photon and piezo technology; and that the experiments can be performed at room temperature. Our study has shown that all components of the setup must be chosen carefully, and that their influences on the reduction point in time must be calculated. Furthermore, one needs good techniques to minimise the setup's interaction with the environment during superposition.

The fact that the observation of deviations from Born's rule requires a specially designed experiment explains why such deviations have not yet become conspicuous. The two discussed realisations of the experiment with the piezo capacitor and the capacitor with movable plates predict quite different reduction points in time (i.e. $\bar{t}_C \approx 1\mu s$ and $\bar{t}_C \approx 100\mu s$), but they have in common that the solid that evolves into the three-state superposition must be fairly small, with a volume on the order of one cubic millimetre.

Our numerical calculations have shown that the approximation formulae derived here are sufficient for the dimensioning of the experiment. These formulae are Equations (21) and (27) for the reduction probability of State 2, and Equations (33)-(35), (37) and (38) for the reduction point in time and the displacement at this point in time of the piezo and the movable plates capacitor. For the dimensioning of the experiment, the experimenter must not perform numerical calculations. The influences of the other components of the setup on the result (such as the photodiodes etc.) can be estimated with the formulae derived in [3].

Critical to the success of the experiment is the minimisation of environmental interaction during superposition to avoid a shortening of the reduction point in time. The switches for disconnecting the voltage supply and the voltmeter from the setup during superposition in Figure 4 can be realised by field effect transistors in enhancement mode. Any possible remaining interactions of such electric circuits with the environment should be analysed in detail.

It is exciting whether we will obtain new results with the proposed experiments, shedding more light on the riddle of wavefunction collapse.

Acknowledgements

I would like to thank my friend Christoph Lamm for supporting me and for proofreading the manuscript.

References

- [1] **G. Quandt-Wiese**, The Dynamical Spacetime approach to wavefunction collapse in a nutshell, <http://quandt-wiese.de/onewebmedia/DynamicalSpacetimeApproach.pdf>
- [2] **G. Quandt-Wiese**, Towards a theory of wavefunction collapse Part 2: Collapse as abrupt reconfigurations of wavefunction's evolution in a dynamically expanding spacetime, *arXiv:1701.01765* (2017)
- [3] **G. Quandt-Wiese**, Diósi-Penrose criterion for solids in quantum superpositions and a single-photon detector, *arXiv:1701.00353* (2017)
- [4] **G. Quandt-Wiese**, Towards a theory of wavefunction collapse Part 1: How the Diósi-Penrose criterion and Born's rule can be derived from semiclassical gravity and how the Diósi-Penrose criterion can be relativistically generalised with the help of the Einstein-Hilbert action, *arXiv:1701.00343* (2017)
- [5] **L. Diósi**, Models for universal reduction of macroscopic quantum fluctuations, *Phys. Rev. A*, 40, 1165-1174 (1989)
- [6] **R. Penrose**, On gravity's role in quantum state reduction, *Gen. Rel. Grav.*, 28, 581-600 (1996)
- [7] **A. Bassi, G. C. Ghirardi**, Dynamical Reduction Models, *Phys. Rept.*, 379, 257 (2003), *arXiv:quant-ph/0302164*
- [8] **W. Marshall, C. Simon, R. Penrose, D. Bouwmeester**, Towards quantum superpositions of a mirror, *Phys. Rev. Lett.*, 91, 130401 (2003), *arXiv:quant-ph/0210001*
- [9] **L. Rosenfeld**, *Nucl. Phys.*, 40, 353 (1963)
- [10] **C. Møller**, in *Les Theories Relativistes de la Gravitation, Colloques Internationaux CNRS 91*, edited by A. Lichnerowicz and M.-A. Tonnelat, CNRS, Paris (1962)
- [11] **M. Bahrami, A. Großardt, S. Donadi, A. Bassi**, The Schrödinger-Newton equation and its foundations, *New J. Phys.*, 16, 115007 (2014), *arXiv:1407.4370*
- [12] **J. R. van Meter**, Schrödinger-Newton "collapse" of the wave function, *Class.Quant.Grav.*, 28, 215013 (2011), *arXiv:1105.1579*
- [13] **R. Penrose**, On the Gravitization of Quantum Mechanics 1: Quantum State Reduction, *Found Phys.*, 44, 557-575 (2014)
- [14] **S. Carlip**, Is Quantum Gravity Necessary?, *Class. Quant. Grav.*, 25, 154010 (2008), *arXiv:0803.3456*
- [15] **M. Bahrami, A. Bassi, S. McMillen, M. Paternostro, H. Ulbricht**, Is Gravity Quantum?, *arXiv:1507.05733* (2015)
- [16] **L. Diósi**, Intrinsic time-uncertainties and decoherence: comparison of 4 models, *Brazilian Journal of Physics*, 35, 260-265 (2005)
- [17] **G. Ribordy, J.D. Gautier, H. Zbinden, N. Gisin**, Performance of InGaAs/InP avalanche photodiodes as gated-mode photon counters, *Applied Optics*, 37, 2272-2277 (1998)

- [18] **S. Cova, S. Ghioni, A. Lacaia, C. Samori, F. Zappa**, Avalanche photodiodes and quenching circuits for single-photon detection, *Applied Optics*, 35(12), 1956-1976 (1996)
- [19] **PI Ceramic GmbH**, Catalog on PI Piezoelectric Ceramic Products, <http://www.piceramic.com>
- [20] **PI Ceramic GmbH**, Catalog on Piezoelectric Actuators, <http://www.piceramic.com>
- [21] See e.g. wikipedia or other sources in the internet